ENN Encyclopedia of Nanoscience and Nanotechnology
www.aspbs.com/enn

Superparamagnetic Iron Oxide Nanoparticles

Kyoungja Woo

Nano-Materials Research Center, Korea Institute of Science and Technology, 39-1 Hawolkok-dong, Sungbook-gu, Seoul, 136-791, Korea

CONTENTS

1. INTRODUCTION

Magnetic iron oxide nanoparticles have recently attracted a great deal of attention because of their unique size-dependent properties, which are not observed in the molecular or bulk phases. The size-dependent properties implicate a high potential for technological applications such as high-density magnetic recording media, clinical uses, sensors, and catalysts [1–7]. Recent advances in the production of monodisperse superparamagnetic iron oxide nanoparticles (SPIONs) have accelerated the emergence of surface modification chemistry and nanostructure construction for technological applications.

The SPIONs at atmospheric condition generally include Fe_3O_4 (magnetite) and γ-Fe_2O_3 (maghemite) nanoparticles less than 20 nm. The other polymorphic phases of iron oxide nanoparticles such as Fe_xO (wüstite for $0.84 < x < 0.95$) or α-Fe_2O_3 (hematite) are unstable to oxidation [8] or very weakly ferromagnetic or superparamagnetic [9–11]. The saturation magnetization of Fe_3O_4 and γ-Fe_2O_3 is 80–100 $Am^2\ kg^{-1}$ and is two orders of magnitude higher than that of hematite [1]. So, the scope of this review will be limited to only discrete, monodisperse, and superparamagnetic Fe_3O_4 and γ-Fe_2O_3 nanoparticles, of which sizes are less than 20 nm. Synthesis, surface modification, and applications of SPIONs will be reviewed.

2. PREPARATION

Various methods have been developed for the preparation of iron oxide nanoparticles. Generally, the thermal chemical synthesis in the presence of surfactants provides the monodisperse SPIONs without aggregation compared to the other methods.

2.1. Thermal Decomposition of an Organometallic Precursor

The thermal decomposition of an organometallic precursor in hot surfactant solution has been developed for the synthesis of highly monodisperse SPIONs, satisfying the requirements of new trends for the technological applications.

2.1.1. Thermal Decomposition of an $FeCup_3$ Single-Source Precursor

The thermal decomposition of an iron organometallic precursor and its possibility to prepare monodisperse SPIONs were introduced by Alivisatos and coauthors [12]. The direct decomposition of an $FeCup_3$ (Cup: N-nitrosophenylhydroxylamine, $C_6H_5N(NO)O^-$) single precursor in hot surfactant solution yielded γ-Fe_2O_3 nanocrystals that were 5.2 nm in average size. In the case of preparation with an additional secondary injection, each subsequent extraction of the reaction precipitate resulted in approximately a 1 nm increase in the average particle diameter. Consequently, the fifth fraction contained γ-Fe_2O_3 nanocrystals which were 10.0 ± 1.5 nm in diameter (Figure 1). By using size-selective precipitation, it was suggested to achieve size distributions of less than 10% standard deviation.

2.1.2. Thermal Decomposition of $Fe(CO)_5$ and/or Iron–Oleate Complex

The first synthesis of monodisperse SPIONs without a size-selection process (standard deviation < 5%) was pioneered

ISBN: 1-58883-188-4

Encyclopedia of Nanoscience and Nanotechnology
Edited by H. S. Nalwa
Volume 23: Pages (487–511)

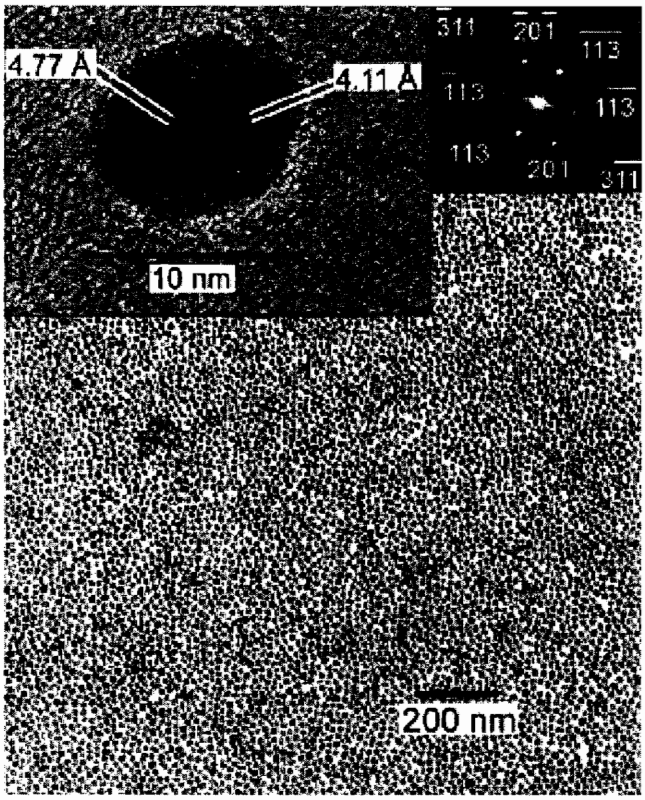

Figure 1. Low-resolution transmission electron microscopy (TEM) image of a monolayer of individual γ-Fe_2O_3 nanocrystals (10.0 ± 1.5 nm) covering an area bigger than 2 μm^2. Top left: high-resolution TEM (HRTEM) image of one of the nanocrystals in this sample. The indicated lattice plane distances correspond to the (113) and (201) lattice planes of tetragonal γ-Fe_2O_3 with ordered superlattice of the cation vacancies. Top right: Fast Fourier Transform (FFT) of the high-resolution TEM image looking down the zone axis. Reprinted with permission from [12], J. Rockenberger et al., *J. Am. Chem. Soc.* 121, 11595 (1999). © 1999, American Chemical Society.

by Hyeon et al. [13, 14] from the thermal decomposition of $Fe(CO)_5$ in octyl ether containing oleic acid, followed by oxidation of the obtained iron nanoparticles with trimethylamine oxide, which can lead to high-quality monodisperse γ-Fe_2O_3 nanospheres ranging from 4 to 11 nm in diameter. Larger monodisperse SPIONs were produced by increasing the molar ratio of the surfactant to the precursor from 1 up to 3. Additional secondary injection resulted in an increase in the average particle diameter. However, the maximum diameter which can be obtained by repeated additional injection was limited to 16 nm. The transmission electron microscopy (TEM) image and X-ray diffraction (XRD) pattern of 11 nm particles in Figures 2 and 3 show a highly monodisperse and crystalline γ-Fe_2O_3 phase. The magnetization vs. temperature curves (Figure 4) of 4, 13, and 16 nm particles all displayed the blocking temperature below room temperature at 25, 185, and ~290 K. This method has been referenced broadly since it is relatively easy to work with and yields high-quality SPIONs.

Various SPIONs were also produced and characterized by modifying the described reference method of Hyeon

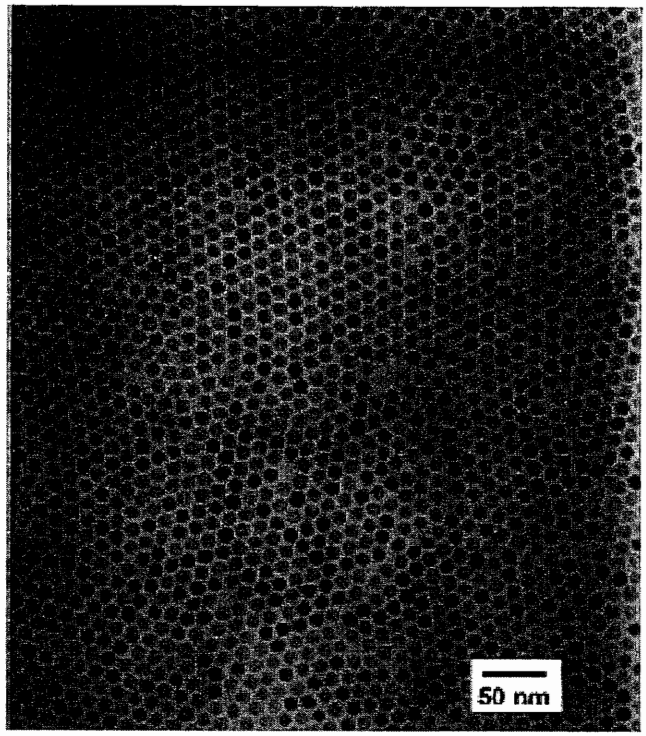

Figure 2. Transmission electron microscopy (TEM) image of a two-dimensional hexagonal assembly of 11 nm γ-Fe_2O_3 nanocrystallites. Reprinted with permission from [13], T. Hyeon et al., *J. Am. Chem. Soc.* 123, 12798 (2001). © 2001, American Chemical Society.

et al. [13], and the mechanistic studies have been reported. The standard XRD patterns of γ-Fe_2O_3 and Fe_3O_4 are nearly identical. Both phases have the inverse spinel structure, in which Fe^{2+} ions occupy the octahedral sites and Fe^{3+} ions occupy both the octahedral and tetrahedral sites in Fe_3O_4, whereas the extra charge is compensated for by a cation vacancy in γ-Fe_2O_3 [1]. Therefore, phase characterization by only the TEM, XRD, X-ray photoelectron spectroscopic (XPS), and Raman spectroscopic data may not be

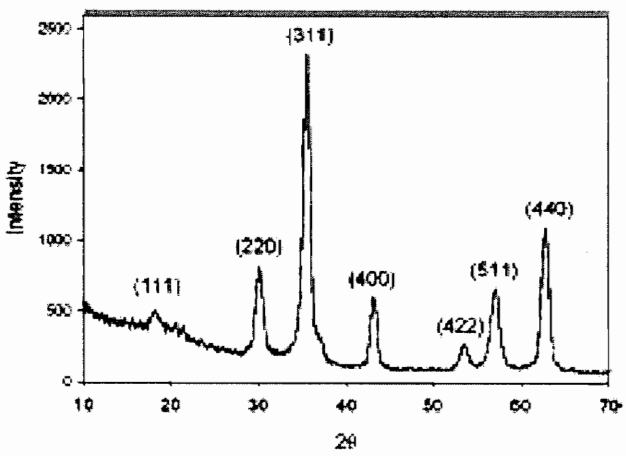

Figure 3. X-ray diffraction (XRD) pattern of 11 nm γ-Fe_2O_3 nanocrystallites. Reprinted with permission from [13], T. Hyeon et al., *J. Am. Chem. Soc.* 123, 12798 (2001). © 2001, American Chemical Society.

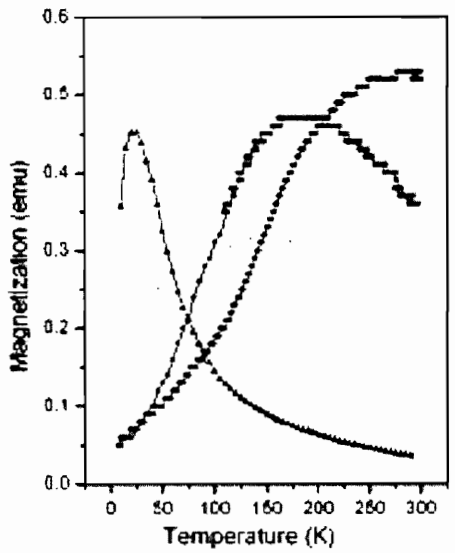

Figure 4. Magnetization versus temperature for 4 nm (triangles), 13 nm (squares), and 16 nm (circles) γ-Fe_2O_3 nanocrystallites with zero-field cooling at the applied magnetic field of 100 Oe. The magnetic studies were conducted with a Quantum Design (MPMS) superconducting quantum interference device (SQUID) magnetometer. Reprinted with permission from [13], T. Hyeon et al., *J. Am. Chem. Soc.* 123, 12798 (2001). © 2001, American Chemical Society.

enough to differentiate γ-Fe_2O_3 from the Fe_3O_4 phase in case of a mixed-phase SPION. The Mossbauer data about the iron nuclear environment or X-ray absorption spectroscopy (XAS) combined with X-ray magnetic circular dichroism (XMCD) data give more accurate information about the phase of SPIONs. Actual examples will follow below.

An easy preparation of monodisperse 5 and 11 nm γ-Fe_2O_3 and 19 nm Fe_3O_4 particles was made by Woo et al. [15] by thermal decomposition of $Fe(CO)_5$ with oleic acid in the presence of residual oxygen of the system and by consecutive aeration. The investigations by Mössbauer spectroscopy (Figure 5 and Table 1), a superconducting quantum interference device (SQUID) magnetometer, and optical microscopy (Figure 6) in addition to the XRD pattern showed that the particle behavior is size dependent and superparamagnetic with and without interparticle interactions in the respective 11 and 5 nm γ-Fe_2O_3 particles and ferromagnetic in 19 nm Fe_3O_4 particles. For the aerated 5 and 11 nm particles, the isomer shift values suggested that the valence state is all +3, and so the phase is γ-Fe_2O_3. In one of the two fitted sextets at 300 K for 19 nm particles, the isomer shift value 0.56 mm/s relative to Fe metal corresponds to $Fe^{2.5+}$ on octahedral sites of Fe_3O_4 [1]. It was found that the smaller nanoparticles prefer the γ-Fe_2O_3 phase, while the larger nanoparticles prefer the Fe_3O_4 phase. Hyeon and coauthors [16] investigated their reaction procedure further and improved it to produce a 1 nm increase in the average particle diameter with a continuous size spectrum of 6–13 nm (Figure 7) after the secondary injection. The separation of the nucleation and growth processes played a key role in controlling the particle size with a 1 nm increment. From the X-ray absorption spectroscopy and X-ray magnetic circular dichroism results (Figure 8), they made a quantitative estimation of the compositions of the iron oxide nanocrystals in the form of $(\gamma\text{-}Fe_2O_3)_{1-x}$ $(Fe_3O_4)_x$. The fraction of the Fe_3O_4 component gradually increases with increasing particle size from 0.20 to 0.65. The broader-than-expected magnetic susceptibility data for monodisperse particles demonstrated the strong dipolar interaction in SPIONs.

The previous methods of SPION preparation starting with $Fe(CO)_5$ include the decomposition reactions of two different complexes, $Fe(CO)_5$ and iron–oleate complexes, at different temperatures. Starting with the iron–oleate complex prepared by the reaction of iron chloride ($FeCl_3{\cdot}6H_2O$) and sodium oleate, Hyeon and coauthors [17] reported ultra-large-scale synthesis (40 g) of monodisperse SPIONs with sizes of 5, 9, 12, 16, and 22 nm using different solvents. The refluxed reaction using a solvent with higher boiling point produces larger SPIONs. Here again, the fraction of the Fe_3O_4 component in the form of $(\gamma\text{-}Fe_2O_3)_{1-x}$ $(Fe_3O_4)_x$ nanocrystals gradually increases with increasing particle size from 0.20 to 1.0.

Cheon et al. [18] reported the shape evolution of single-crystalline γ-Fe_2O_3 nanocrystals by thermal decomposition of $Fe(CO)_5$ using a dodecylamine (DDA) capping ligand under aerobic conditions. Monodisperse γ-Fe_2O_3 nanocrystals were obtained after the shape selection process of a product mixture of diamond-, sphere-, and triangle-shaped nanocrystals. 12 nm sphere-shaped nanocrystals were superparamagnetic, and 50 nm hexagon-shaped nanocrystals were ferromagnetic. The same reaction condition except using a trioctylphosphine (TOPO) capping ligand instead of DDA formed smaller SPIONs of approximately 6 nm (standard deviation = 5.1%).

Some mechanistic studies have been reported for the synthesis of SPIONs using an $Fe(CO)_5$ precursor. By separating the nucleation and growth processes, Hyeon and coauthors [16] showed the particle size control with a 1 nm increment. Monodisperse 6 nm γ-Fe_2O_3 particles were used as nuclei, and a secondary injected iron–oleate complex was utilized for growing. Teng et al. [19] studied the effects of surfactants and synthetic conditions on the sizes of monodisperse iron oxide nanoparticles. They extended the lower limit of monodisperse particle size down to 3 nm by a reaction at 200°C for 1 h using stearic acid instead of oleic acid, and the higher limit up to 25 nm by a reaction at 275°C for 2 h using oleic acid without secondary injection of the precursor. At this temperature, the minimum molar ratio of surfactant:$Fe(CO)_5$ for monodispersity was 3. This reaction temperature of 275°C is contrasted with the others, which are around 303°C during reflux.

Alivisatos and coauthors [20] monitored the formation of SPIONs, initiated from the coinjection of $Fe(CO)_5$ and 3-chloro peroxybenzoic acid (or *meta*-chloro peroxybenzoic acid, mCPBA) solution to a dioctyl ether solution of tridecanoic acid at 293°C, which is accompanied by a color change, via in situ UV-vis spectroscopy. The time dependence of the absorbance (Figure 9a) at 440 nm after coinjection pointed out the presence of a delayed nucleation process and provided information about induction time. No temperature variation was observed once the solution recovered its initial temperature after a few minutes of injection (Figure 9b). The dependence of the induction

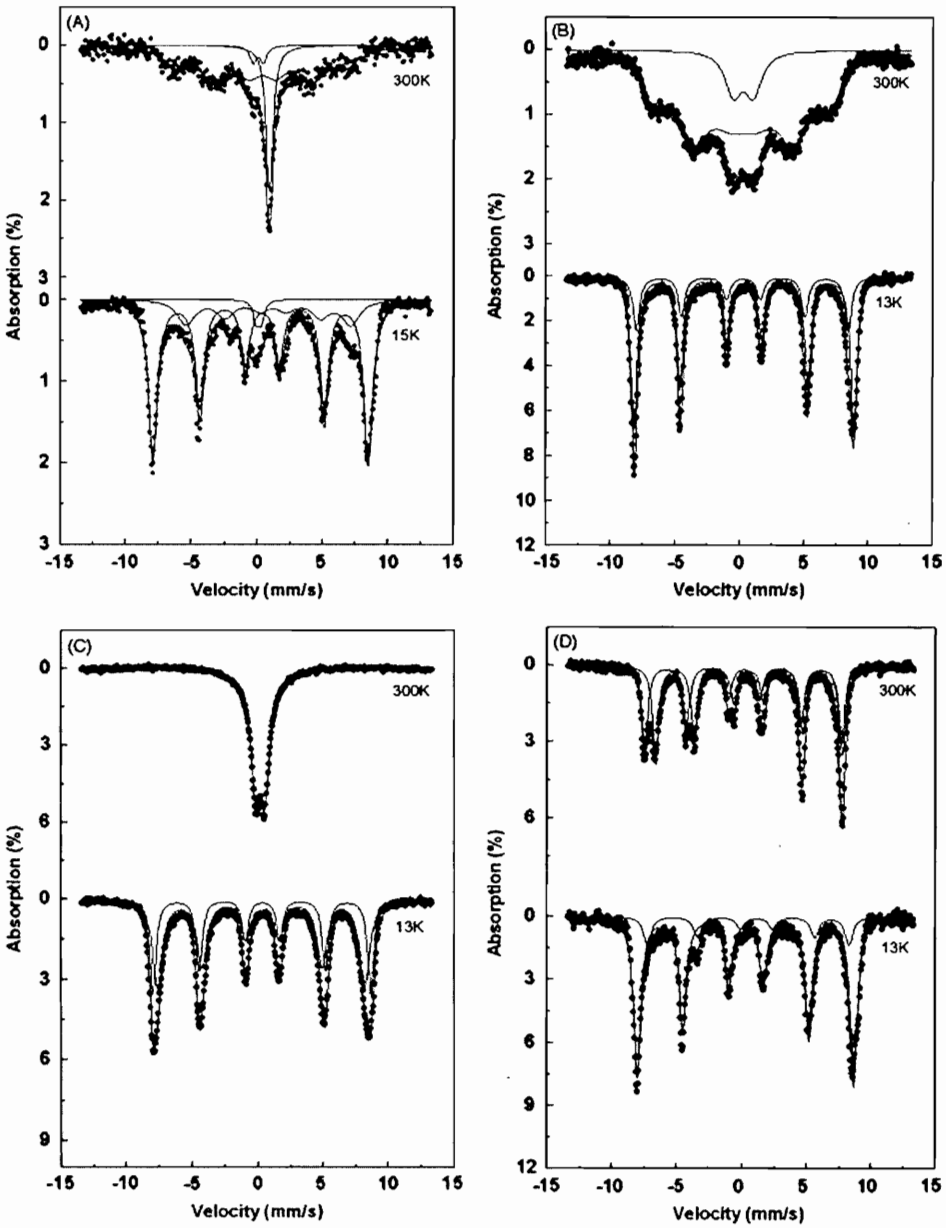

Figure 5. Mössbauer spectra of iron oxide nanoparticles: (a) intermediate 11 nm, and aerated (b) 11 nm, (c) 5 nm, and (d) 19 nm. Reprinted with permission from [15], K. Woo et al., *Chem. Mater.* 16, 2814 (2004). © 2004, American Chemical Society.

time as a function of the iron molar concentration showed that the reaction occurs much faster as the iron concentration is increased and resultantly produces smaller particles (Figure 9c). The retardation of the nucleation is induced by the fatty acid surfactant, which strongly stabilizes the monomer in solution. The delayed nucleation results in a very pronounced monomer supersaturation after the induction time. As a consequence, the presence of monodisperse nuclei and a fast growth regime are responsible for the formation of nanocrystals with nearly monodisperse size and anisotropic shape (nanodisks in this specific case). Under the adopted conditions, the particle size distribution was getting broader as the time elapsed. The crystalline phase of the SPIONs is dependent on the oxidation condition. The decomposition of the oxidizer mCPBA is faster than that of the iron precursor, so that the most effective method to obtain iron oxide nanocrystals with the desired oxidation state (Fe_3O_4. γ-Fe_2O_3, or a mixture of iron oxide) is the sequential injection of oxidizer at different stages of decomposition of the iron precursor.

Synthesis of monodisperse SPIONs (2.5 or 5 nm Fe–Fe_3O_4 core–shell nanoparticles) was reported by Sun and coauthors [21] via thermal decomposition of $Fe(CO)_5$ with an oleylamine ligand in octadecene, followed by controlled oxidation with trimethylamine oxide and then annealing at 400°C and 500°C under Ar. The crystalline Fe_3O_4 shell dramatically increases the chemical stability of core–shell structured SPIONs, whereas the amorphous Fe_3O_4 shell does

Table 1. Analyzed results of Mössbauer spectra for iron oxide nanoparticles.

Particle size (nm)	Temp (K)	Fitted spectrum	Hyperfine field (T)	Quadruple splitting (mm/s)	Isomer shift (mm/s)	Line width (mm/s)	Area (%)	Fe ion state
5[a]	300	doublet		0.71	0.20	0.93	100	+3
5[a]	13	sextet	51.7	0.00	0.35	0.56	40.3	+3
		sextet	49.0	0.02	0.31	0.90	59.7	+3
11[b]	300	sextet	40.4	0.04	0.34	2.17	75.2	+3
		singlet		0.02	0.93	0.61	21.5	+2
		doublet		0.70	0.05	0.37	3.3	
11[b]	15	sextet	51.0	0.04	0.36	0.82	74.6	+3
		sextet	39.1	0.16	1.04	1.62	22.0	+2
		doublet		0.38	0.13	0.73	3.4	
11[a]	300	sextet	41.8	0.02	0.23	1.73	87.6	+3
		doublet		1.54	0.26	1.53	12.4	+3
11[a]	13	sextet	52.8	0.02	0.35	0.59	73.6	+3
		sextet	50.9	0.02	0.26	0.60	26.4	+3
19[a]	300	sextet	47.0	0.02	0.14	0.58	47.6	+3
		sextet	44.7	0.03	0.56	0.58	52.4	+2.5
19[a]	13	sextet	51.8	0.01	0.33	0.67	84.1	+3
		sextet	48.2	0.03	0.83	0.70	15.9	+2

[a] Aerated particles.
[b] Intermediate particles.
Source: Reprinted with permission from [15]. K. Woo et al., *Chem. Mater* 16, 2814 (2004). © 2004, American Chemical Society.

not protect the Fe core from oxidation. Similar synthesis of monodisperse SPIONs (8 nm Fe_3O_4 and 11 nm Fe–γ-Fe_2O_3 core–shell nanoparticles) via an iron–oleylamine complex in octadecene was monitored by Yu et al. [22] using TEM and in situ Fourier transform infrared (FTIR) spectroscopy at specified temperature intervals (Figure 10). The axial and equatorial CO absorption bands at 2020 and 1997 cm^{-1} of trigonal bipyramidal $Fe(CO)_5$ decreased, and two absorption bands emerged at 1927 and 1897 cm^{-1} after heating for 1 h at 90°C. This was supported by the reduced absorption intensity of Fe–C–O bending modes at 635 and 615 cm^{-1}. After heating at 170°C and 200°C, an absorption band at 1970 cm^{-1} emerged, whereas the characteristic absorption bands of CO stretching and Fe–C–O bending modes faded. The bands at 1970 cm^{-1} dramatically decreased and disappeared after heating at 240°C and 270°C, respectively. Yu et al. [22] suggested that the iron oleylamine complex formed via substituting some CO groups of $Fe(CO)_5$ with oleylamine by heating the reaction solution up to 200°C. Thermal decomposition of the iron oleylamine complex at a higher temperature led to the formation of iron nanoparticles, which were oxidized to iron oxide on exposure to residual oxygen. As the molar ratio of oleylamine:$Fe(CO)_5$ reduced from 5 to 3 to 1, the particle size increased from 8 to 11 to 17 nm in that order. A different kind of core–shell nanoparticle, 13.5 nm Cr–γ-Fe_2O_3, was prepared by one-pot decomposition of a 9:1 $Cr(CO)_6$:-$Fe(CO)_5$ mixture using Pluronic F127 as a surfactant in mesitylene [23]. The small Fe clusters formed from $Fe(CO)_5$ decomposition at a much lower temperature catalyze the decomposition of $Cr(CO)_6$ at a higher temperature. The resulting Cr core is then used as a nucleation seed to form an Fe shell layer, which oxidizes to γ-Fe_2O_3.

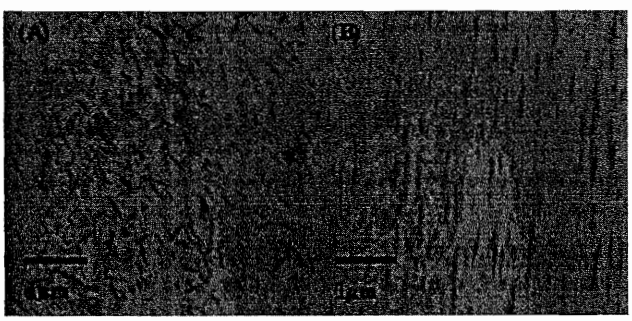

Figure 6. Optical microscopic images of 11 nm intermediate particles: (a) without and (b) with an external magnetic field. Reprinted with permission from [15], K. Woo et al., *Chem. Mater.* 16, 2814 (2004). © 2004, American Chemical Society.

O'Brien and coauthors [8] investigated the synthesis and characterization of Fe_xO nanocrystals from $Fe(CO)_5$ in the presence of an oleic acid capping ligand and dioctyl ether solvent. Tight control over temperature allows the syntheses of cubic or faceted Fe_xO nanocrystals with narrow size distributions by a selective oxidation route of $Fe(CO)_5$ with pyridine *N*-oxide, which possesses lower oxidation potential compared to trimethylamine oxide. Higher reaction temperatures (>300°C) yield Fe_3O_4 and α–Fe by disproportionation of the Fe_xO particles, whereas lower reaction temperatures (~250°C) produce Fe_3O_4 or γ-Fe_2O_3.

O'Brien and coauthors [24, 25] thoroughly investigated the surface of the SPIONs which were prepared in the presence of oleic acid via nuclear magnetic resonance (NMR), infrared (IR), and mass spectroscopy. The ^1H NMR of γ-Fe_2O_3 (Figure 11b) is different from that of pure oleic acid A. B shows a lack of vinyl and allyl proton resonances, which appear at 5.5 and 2.0 ppm in the spectrum of pure oleic acid, suggesting the reduction of the oleic acid double bond during nanocrystal synthesis. The ligand removed from the nanocrystal surface was no longer oleic acid. The IR spectrum (Figure 12a) of γ-Fe_2O_3 shows a carboxylate (COO^-) stretch at 1527 and 1430 cm^{-1}, whereas ligand B stripped from A displays a significant carbonyl stretch

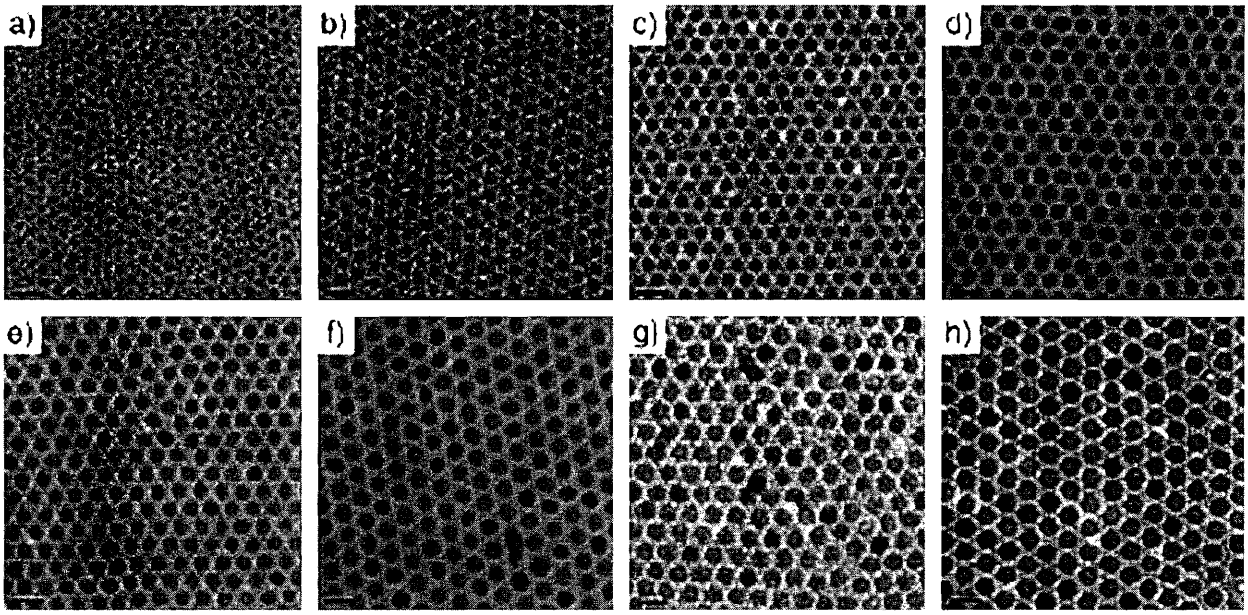

Figure 7. Transmission electron microscopy (TEM) images of (a) 6 nm, (b) 7 nm, (c) 8 nm, (d) 9 nm, (e) 10 nm, (f) 11 nm, (g) 12 nm, and (h) 13 nm air-oxidized iron oxide nanoparticles showing the 1 nm level increments in diameter. Reprinted with permission from [16], J. Park et al., *Angew. Chem. Int. Ed.* 44, 2872 (2005). © 2005, Wiley-VCH.

centered at 1710 cm^{-1}, indicating carboxylate complexation to the iron oxide nanocrystals. The weak vinyl C-H stretch located at 3003 cm^{-1} indicates that there is only a trace amount of oleic acid in A and B compared to free ligand C. Mass data evidenced for the formation of a species possessing the composition of oleic acid plus an additional O atom. If oleic or elaidic acid (the trans isomer of oleic acid) is heated slowly to 350°C, a similar loss of unsaturation is observed by ^1H NMR and FTIR, indicating that the configuration about the double bond is not important in this transformation. The nanoparticles produced using stearic acid [$CH_3(CH_2)_{16}COOH$] or 1-octadecanol [$CH_3(CH_2)_{16}COH$] instead of oleic acid are of irregular shape and low monodispersity. The significance of the carboxylic acid head group in facilitating the uniform nucleation and growth of nanocrystals is clarified by substituting methyl oleate (instead of oleic acid), which exhibits poor yield and polydispersity. Their overall results suggested that the presence of oleic acid is critical in the synthesis of stable, monodisperse SPIONs.

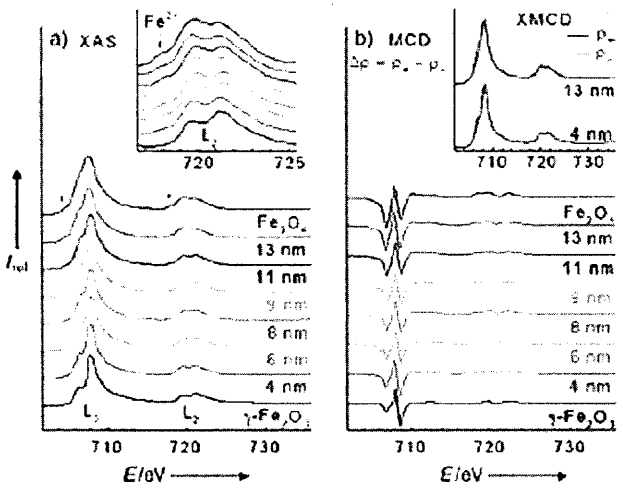

Figure 8. Fe $L_{2,3}$ edge (a) X-ray absorption spectroscopy (XAS) and (b) X-ray magnetic circular dichroism (XMCD) spectra of 4, 6, 8, 9, 11, and 13 nm iron oxide nanocrystals compared with those of bulk reference materials (γ-Fe_2O_3 and Fe_3O_4). The magnified L_2 region XAS spectra of the nanocrystals and XMCD spectra of the 4 and 13 nm nanocrystals are shown in the insets of (a) and (b), respectively. Reprinted with permission from [16], J. Park et al., *Angew. Chem. Int. Ed.* 44, 2872 (2005). © 2005, Wiley-VCH.

2.1.3. Thermal Decomposition of $Fe(acac)_3$, $Fe(acac)_2$, or $Fe(OAc)_2$

Sun and Zeng [26] demonstrated the first synthesis of monodisperse Fe_3O_4 nanoparticles (standard deviation <5%) from a high-temperature reaction of $Fe(acac)_3$ in phenyl ether in the presence of alcohol, oleic acid, and oleylamine, as shown in Scheme 1. Larger monodisperse Fe_3O_4 nanoparticles up to 20 nm were synthesized with the smaller nanoparticles as seeds. All these nanoparticles were superparamagnetic. The TEM and XRD data shown in Figures 13 and 14 indicate single-crystalline SPIONs and phase transformation of 16 nm Fe_3O_4 (Figure 14d) into either γ-Fe_2O_3 (Figure 14e) or α–Fe (Figure 14f) nanoparticles by O_2 oxidation at 250°C or by reduction under Ar + 5% H_2 at 400°C, respectively. They also indicated that using $Fe(acac)_2$ instead of $Fe(acac)_3$ gave the same result. This method has been a broad reference for the synthesis of high-quality Fe_3O_4 SPIONs. The mechanism leading to Fe_3O_4 under this reaction condition is not clear yet. X-ray diffraction profile and high-angle annular dark-field images

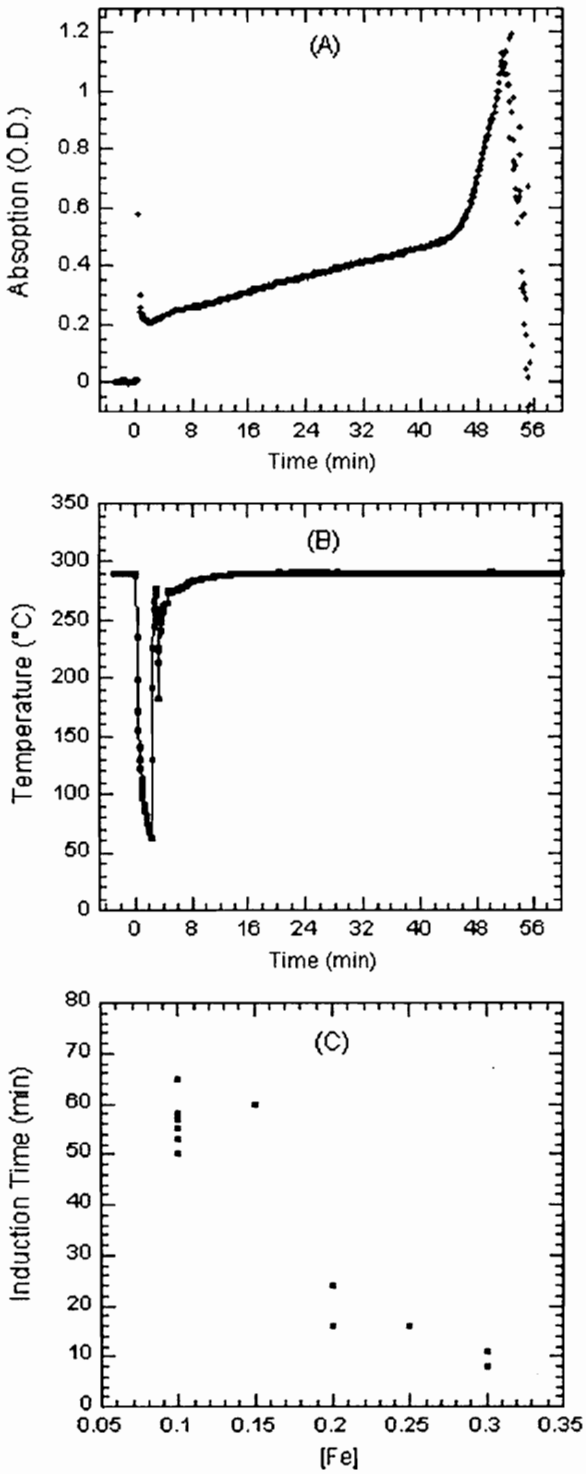

Figure 9. Optical density of the solution collected in situ at 440 nm during a typical synthesis carried out with (a) molar ratios of $Fe(CO)_5$:mCPBA = 1:1.5 and (b) corresponding temperature variation. The time = 0 corresponds to the injection time; the induction time for particle formation under these conditions is about 1 h. The dependence of the induction time on the iron precursor molar concentration is reported in (c). Reprinted with permission from [20], M. Casula et al., *J. Am. Chem. Soc.* 128, 1675 (2006). © 2006, American Chemical Society.

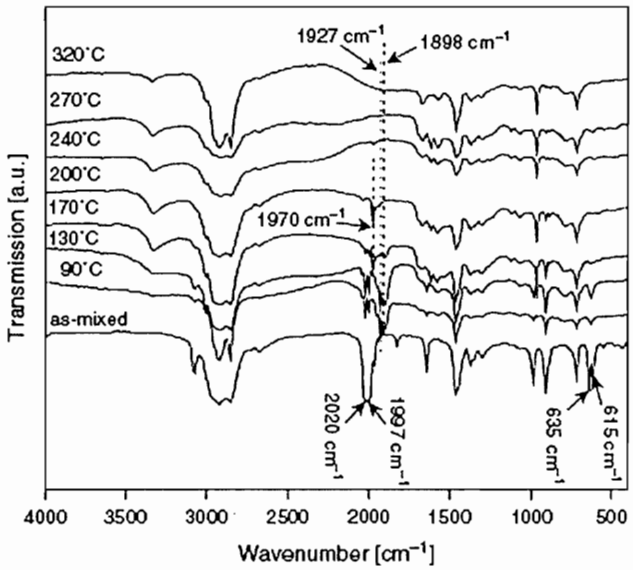

Figure 10. Fourier transform infrared (FTIR) spectra of the samples taken at various temperatures from the reaction solution during the synthesis of iron oxide nanoparticles. Reprinted with permission from [22], S. Yu et al., *J. Nanosci. Nanotechnol.* 6, 2135 (2006). © 2006, American Scientific Publishers.

of Fe_3O_4 SPIONs prepared by this method gave evidence of self-assembled arrays with a size of 4 nm [27]. Sun et al. [28] further investigated the synthesis of monodisperse Fe_3O_4 SPIONs by the high-temperature reaction of $Fe(acac)_3$. The higher boiling solvent benzyl ether produces bigger SPIONs, and preheating at 200°C for some time before it is heated to reflux is the key for the monodispersity of nanoparticles. The reaction of the more expensive $Fe(acac)_2$ or $Fe(OAc)_2$ precursors yields no better result than that of $Fe(acac)_3$. The phase transformation of 16 nm Fe_3O_4 to γ-Fe_2O_3 under oxygen at 250°C, and then to α-Fe_2O_3 under Ar at 500°C, was shown. This reaction was

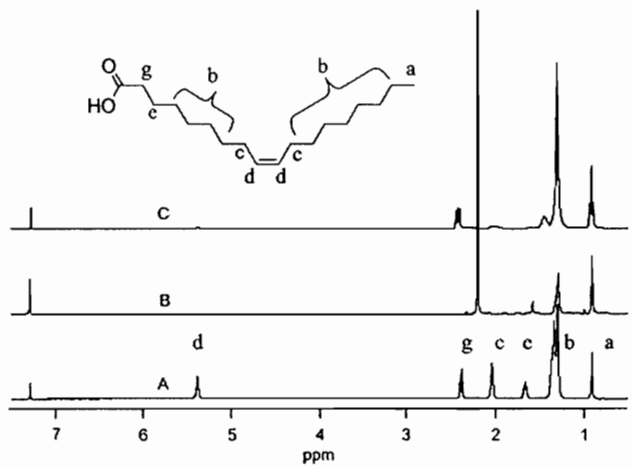

Figure 11. (a) ^1H nuclear magnetic resonance (NMR) of oleic acid, (b) surfactant bound to Fe_2O_3 nanocrystals, and (c) surfactant removed from the Fe_2O_3 surface. Reprinted with permission from [24], A. L. Willis et al., *Chem. Mater.* 17, 5970 (2005). © 2005, American Chemical Society.

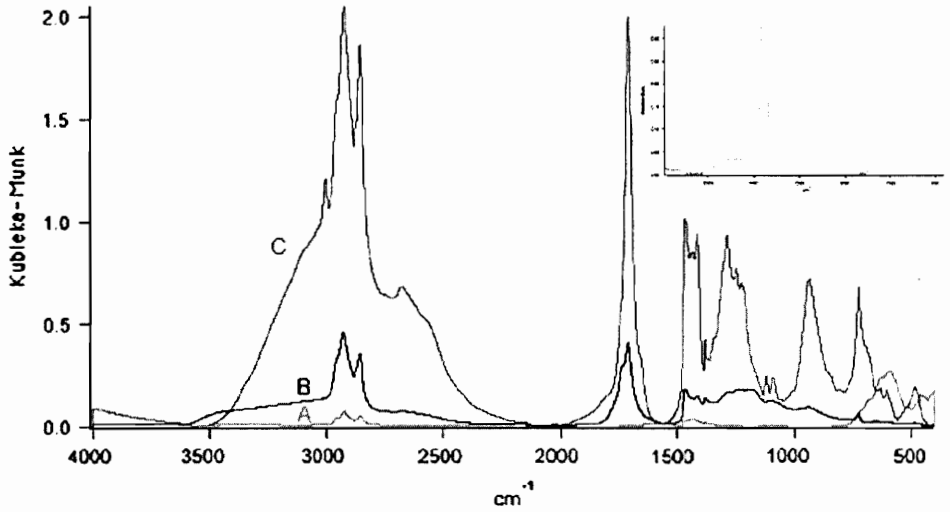

Figure 12. Diffuse Reflectance Infra-red Fourier Transform (DRIFT) infrared (IR) of (a) Fe_2O_3 nanocrystals, (b) stripped surfactant, and (c) oleic acid. Inset shows an enlarged image of spectrum (a). Reprinted with permission from [24], A. L. Willis et al., *Chem. Mater.* 17, 5970 (2005). © 2005, American Chemical Society.

successfully extended to the general synthesis of MFe_2O_4 (M = Fe, Co, and Mn) nanoparticles [28, 29].

O'Brien and coauthors investigated the synthesis and characterization of wüstite (Fe_xO) nanocrystals from $Fe(acac)_2$, $Fe(acac)_3$, $Fe(OAc)_2$, and $Fe(CO)_5$ with pyridine *N*-oxide in the presence of a capping ligand (oleic acid) and organic ether solvent [8]. The decomposition reaction of $Fe(OAc)_2$ at 255°C allows the syntheses of cubic or faceted Fe_xO nanocrystals, with narrow size distributions, which further oxidize to Fe_3O_4 or γ-Fe_2O_3 during isolation. Because of the similarity of the high-temperature reaction products of $Fe(CO)_5$ in the case of oxidation with pyridine *N*-oxide with the decomposition products of $Fe(OAc)_2$, it was assumed that the initial iron particles are oxidized to Fe_xO, which undergoes a subsequent reaction to Fe_3O_4 and α-Fe, as shown in Scheme 2. As described in Section 2.1.2, higher reaction temperatures (>300°C) yield Fe_3O_4 and α-Fe by disproportionation of the Fe_xO particles, whereas lower reaction temperatures (~250°C) produce Fe_3O_4 or γ-Fe_2O_3 nanoparticles.

Li et al. [30] reported the synthesis of Fe_3O_4 SPIONs by thermal decomposition of $Fe(acac)_3$ in 2-pyrrolidone in the presence of monocarboxyl-terminated poly(ethylene glycol) (MPEG–COOH). In this case, it was confirmed by FTIR spectroscopy that both 2-pyrrolidone and MPEG–COOH were complexed to Fe_3O_4 nanoparticles. Monodispersity of these SPIONs was not as good as it was for those synthesized by Sun and Zeng [26]. For example, average 9.8 nm particles showed a standard deviation of 1.4 nm. However, this method showed a possibility for one-pot synthesis of biocompatible SPIONs.

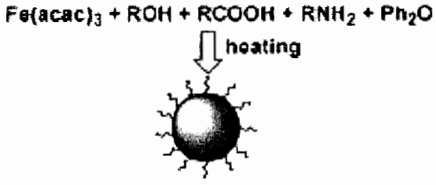

Scheme 1. Simple organic-phase synthesis of magnetic nanoparticles. Reprinted with permission from [26], S. Sun et al., *J. Am. Chem. Soc.* 124, 8204 (2002) © 2002, American Chemical Society.

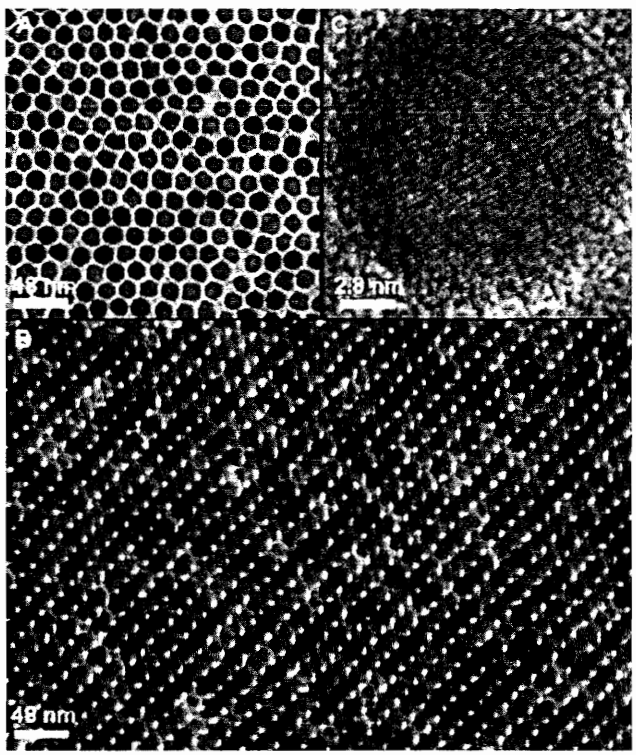

Figure 13. Transmission electron microscopy (TEM) bright field image of 16 nm Fe_3O_4 nanoparticles deposited from their dodecane dispersion on an amorphous carbon surface and dried at 60°C for 30 min: (a) a monolayer assembly, (b) a multilayer assembly, and (c) a high-resolution TEM (HRTEM) image of a single Fe_3O_4 nanoparticle. The images were acquired from a Philips EM 430 at 300 kV. Reprinted with permission from [26], S. Sun et al., *J. Am. Chem. Soc.* 124, 8204 (2002). © 2002, American Chemical Society.

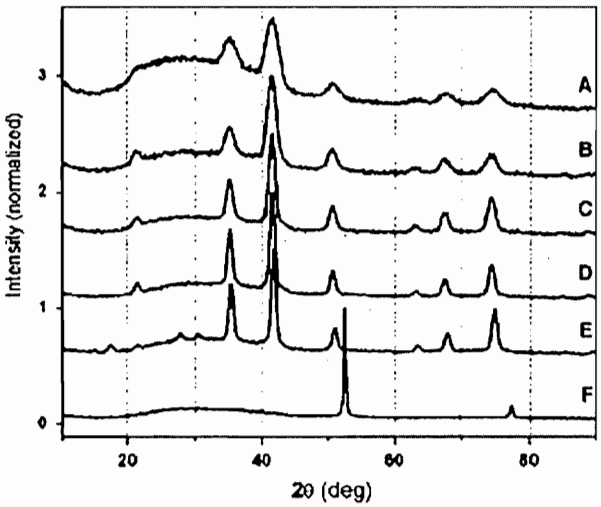

Figure 14. X-ray diffraction (XRD) patterns of (a) 4 nm, (b) 8 nm, (c) 12 nm, and (d) 16 nm Fe_3O_4 nanoparticle assemblies, and a (e) γ-Fe_2O_3 nanoparticle assembly obtained from the oxidation of a 16 nm Fe_3O_4 nanoparticle assembly under oxygen at 250°C for 2 h. (f) A bcc–Fe nanoparticle assembly obtained from the reduction of a 16 nm Fe_3O_4 nanoparticle assembly under Ar + H_2 (5%) at 400°C for 2 h. All samples were deposited on glass substrates from their hexane dispersions. Diffraction patterns were collected on a Simens D-500 diffractometer under Co Kα radiation (λ = 1.788965 Å). Reprinted with permission from [26], S. Sun et al., *J. Am. Chem. Soc.* 124, 8204 (2002). © 2002. American Chemical Society.

2.2. Thermal Treatment of an Iron (Oxy)hydroxide Gel Precursor

Thermal treatment of iron (oxy)hydroxide gel in the presence of oleic acid produces relatively monodisperse SPIONs for technological applications.

A set of monodisperse SPIONs ranging from 7.8 to 17.9 was synthesized from thermal decomposition of Fe(O)OH with oleic acid in the presence of high boiling solvents (1-octadecene or docosane) [31]. The higher boiling solvent produces the bigger sized nanoparticles. The phase of the SPIONs is estimated as a mixture of Fe_3O_4 and γ-Fe_2O_3 from the XRD data. The saturation magnetization and coercive force Hc (77 K) are functions of the particle size and increase with the particle size.

Bourlinos et al. [32] reported the selective preparation of aliphatic acid–capped Fe_3O_4 or γ-Fe_2O_3 SPIONs from iron hydroxide gel, via oxidation with H_2O_2 or $(NH_4)_2S_2O_8$ (better for safety) solutions. Capping with aliphatic acids is established simultaneously in one step by adding a toluene solution of the capping agent and refluxing the resulting biphase system at 95°C. The ferrous hydroxide gel was formed in situ from $FeSO_4 \cdot 7H_2O$ or $(NH_4)_2Fe(SO_4)_2 \cdot 6H_2O$ solution by adding base. Depending on the selected base, KOH and NH_3 produce Fe_3O_4 and γ-Fe_2O_3 SPIONs, respectively. These SPIONs were thoroughly characterized by XRD, FTIR, vibrating sample method (VSM), and Mössbauer data.

Woo at al. [9, 33, 34] reported the sol-gel-mediated synthesis of γ-Fe_2O_3 nanospheres and nanorods. Iron oxyhydroxide gel was prepared from $FeCl_3$ aqueous solution by adding a proton scavenger, propylene oxide, inside the reverse micelle of oleic acid, which constitutes water in oil microemulsion. Depending on the washing condition, nanospheres or nanorods resulted since the washing process controls the amount of capping ligand on the gel surface. Refluxing the gel in tetralin solvent under different conditions yields relatively monodisperse crystalline α- and γ-Fe_2O_3 nanoparticles (Figure 15). The 5.5 nm γ-Fe_2O_3 nanospheres were superparamagnetic, with magnetization of 59 emu/g at 1 T. The 5 × 16 nm (diameter × length) γ-Fe_2O_3 nanorods were superparamagnetic, too, with blocking temperature at around 130 K, which is much higher than that [13] of γ-Fe_2O_3 nanospheres with a similar diameter.

2.3. Other Preparations

Fe_3O_4 nanoparticles commonly have been prepared by coprecipitation from ferric (Fe^{3+}) and ferrous (Fe^{2+}) solution by an addition of alkaline solution [35–37]. The iron oxide particles prepared by this method have been quite limited to meet the requirements for building nanostructures and property control since the reaction rate is too fast to control the size or shape of the particles, besides the aggregation problem. Though the size and shape are not monodisperse, methods have been developed to improve the quality of iron oxide nanoparticles. Coating the coprecipitated Fe_3O_4 particles with oleate or other anionic forms of fatty acids has been reported [38, 39]. The resultant Fe_3O_4 particles showed superparamagnetism and almost immeasurable remanence magnetization and coercivity. Coprecipitated Fe_3O_4 particles in the presence of polymerized lactic acid or starch produced clusters (~80 nm) of iron oxide nanocrystals (~10 nm) or SPIONs with a mean

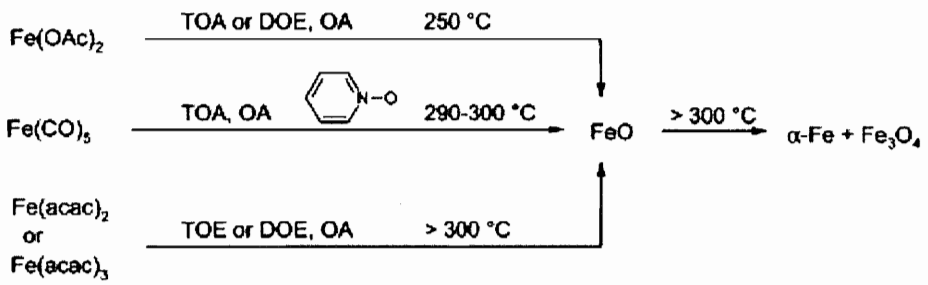

Scheme 2. Different reactions under investigation for the synthesis of wüstite nanocrystals. Reprinted with permission from [8], F. X. Redl et al., *J. Am. Chem. Soc.* 126, 14583 (2004). © 2004, American Chemical Society.

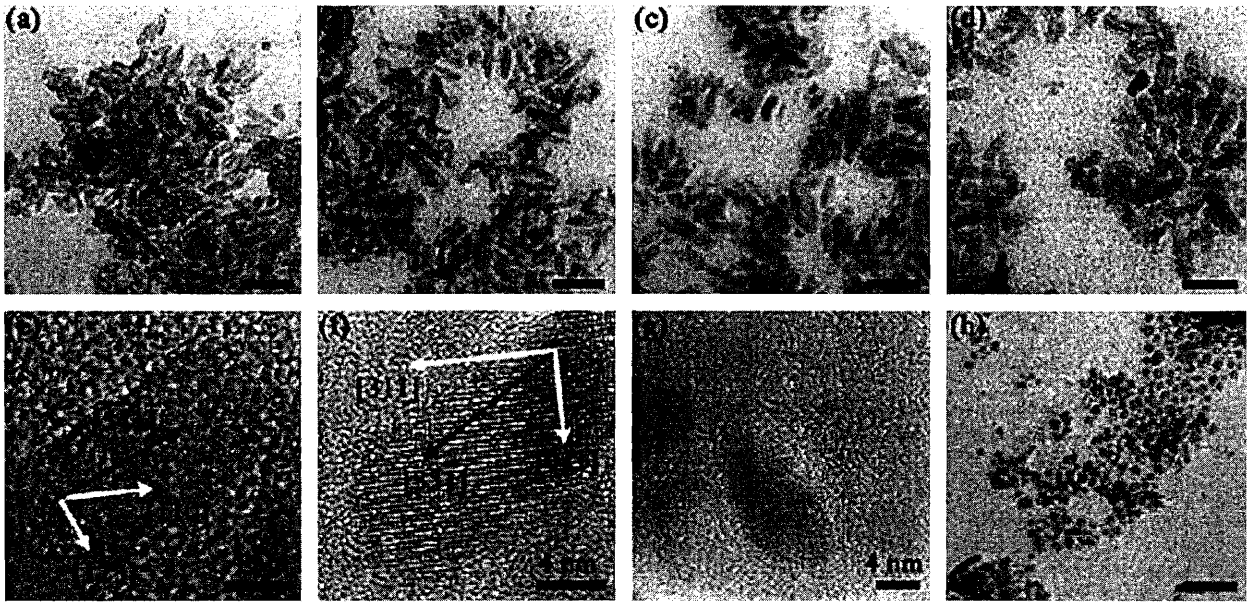

Figure 15. Transmission electron microscopy (TEM) images of (a) α-Fe_2O_3, (b) γ-Fe_2O_3, and (c, d) (α + γ)–Fe_2O_3 nanorods; high-resolution TEM (HRTEM) images of (e) an α-Fe_2O_3 nanorod with a zone axis of [$1\bar{1}1$], (f) a γ-Fe_2O_3 nanorod with a zone of [$\bar{2}33$], and (g) a peanut-shaped γ-Fe_2O_3; and (h) a TEM image of roughly spherical γ-Fe_2O_3 nanoparticles. Unlabeled bars, 30 nm. Reprinted with permission from [33], K. Woo et al., *Adv. Mater.* 15, 1761 (2003). © 2003, Wiley-VCH.

size of 6 nm, embedded inside the polymer chains [40] or in a polymeric starch matrix [41].

Fe_3O_4 SPIONs also can be prepared by a solvothermal reaction (180°C) of Fe powder and $FeCl_3 \cdot 6H_2O$ in a hexane solution containing oleic acid and laurylamine [42]. The solvothermal temperature and consequent aging time were demonstrated to be critical for size distribution.

Template-mediated synthesis produces highly monodisperse iron oxide nanoparticles, though they are contaminated and aggregated after removal of the template. Thus, this method has been used to prepare nonisomorphic iron oxide particles such as nanotubes, which are not commonly available without a template [43, 44].

3. SURFACE MODIFICATION

Surface modification and surface control are of fundamental importance for the technological applications of SPIONs, since the particle behavior and construction of assembled structures depend on their surface properties to a high degree. This review will be categorized according to surface shell material, which is organic or inorganic.

3.1. Inorganic SPION Core--Organic Shell

As-synthesized SPIONs are hydrophobic and quite soluble in nonpolar solvents such as toluene, hexanes, and chloroform, since the SPIONs are coordinated by polar head groups of the surfactant ligands with their nonpolar tails directing outward. The constitution of this nanoparticle is regarded as an inorganic SPION core–organic shell. These hydrophobic SPIONs can be utilized without further surface modification occasionally. However, they usually need surface modification for practically useful technological applications. Surface modification of SPIONs by organic polymers is classified into two categories, covalent conjugation or adsorption, according to its interaction type with organic materials.

3.1.1. Ligand Exchange and Covalent Conjugation of SPIONs to Organic Polymers

For the covalent conjugation of SPIONs to organic polymers, it is necessary that the SPIONs be coated or coordinated by the organic ligand with an available functional group for a bond on the other terminus. The representative available functional groups are amines and carboxylic acids, which make amide bonds readily with prevalent biological or chemical molecules. The organic ligand, which is directly coordinated to SPIONs by a ligand exchange reaction, can be a small bifunctional organic molecule or a dendron and needs further modification by covalent conjugation or by adsorption of an organic polymer for useful application. Sometimes, the organic polymer possessing a coordinating group can be directly exchanged with the ligand on the nanocrystal to make an inorganic SPION core–organic shell.

Peng et al. [45] reported a super-stable, high-quality, Fe_3O_4 nanocrystal core–dendron shell dispersible in both organic and aqueous solutions. They introduced a new class of ligands, poly(ethylene glycol) (PEG)-terminated organic dendrons with a hydroxamic acid group (a known strong-bonding group for bulk iron oxide surfaces [46]) located at the focal point (Figure 16, top left), for stabilizing magnetic oxide nanocrystals, thus producing a SPION core–dendron shell. The asymmetric terminal double bond provides a potential cross-linking or conjugating site for chemical and

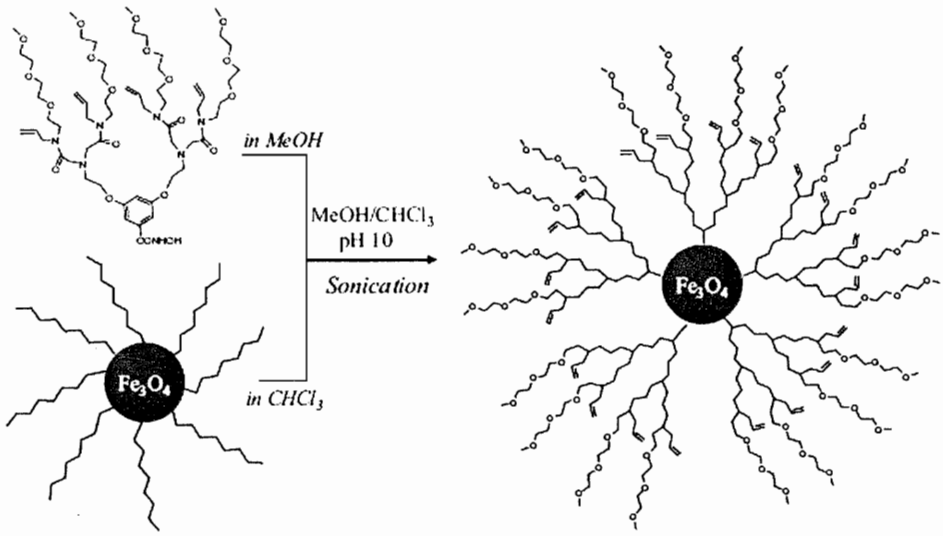

Figure 16. Schematic illustration of the dendron ligand (top left) and the surface–ligand displacement reaction. Note that the structures of the ligands on the surfaces of the nanocrystals are simplified. Reprinted with permission from [45], M. Kim et al., *Adv. Mater.* 17, 1429 (2005). © 2005, Wiley-VCH.

biochemical functionalization. Ligand exchange of the stearate-coated Fe_3O_4 nanocrystals, as shown in Figure 16, produced Fe_3O_4 dendron-nanocrystals with maintained size and size distribution. The well-dispersed TEM image of the Fe_3O_4 dendron-nanocrystals (Figure 17, top right) indicated that no aggregation occurred during and after the ligand exchange. Peng et al. [45] verified that hydroxamic acid, compared with phosphonic acid and carboxylic acid, gave the strongest bonding for the SPIONs by showing a complete surface replacement with hydroxamic acid–based dendron ligands (Figure 17, left panel). The FTIR spectra before and after the ligand exchange showed that the asymmetric $-COO^-$ vibration band centered at about 1527 cm^{-1} almost disappeared after the ligand exchange, and new vibration bands associated with the amide I and II vibrations of hydroxamic acid were observed at 1647 and 1458 cm^{-1}, respectively.

The ligand exchange reaction of surfactant-coated SPION has been explored with various small organic molecules. The ligand exchange of alkylamine-protected γ-Fe_2O_3 SPIONs using functionalized alcohols and diols with dodecyl tails was presented by Rotello and coauthors [47]. The stability of the modified nanoparticles was found to be dependent on the nature of the introduced alcohol: both bidentate surface–ligand bonding and steric blocking by bulky tail groups were necessary to produce systems resistant to agglomeration. The most notable change after ligand displacement was the appearance of a strong absorption at ca. 1050 cm^{-1} arising from C–O single-bond stretching. It was demonstrated that the γ-Fe_2O_3 core functionality was

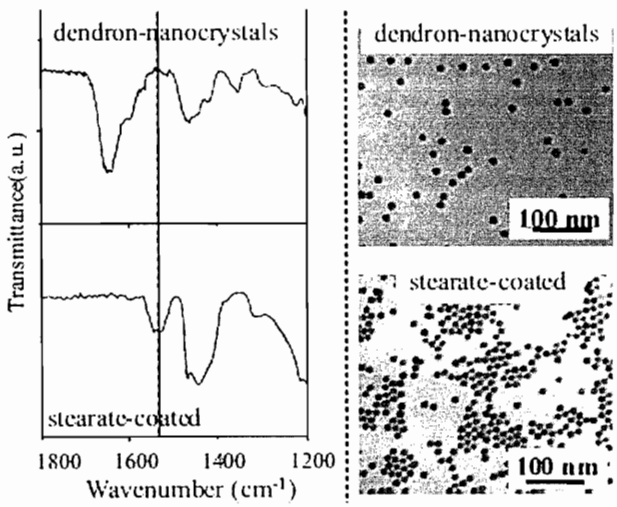

Figure 17. Left panel: Fourier transform infrared (FTIR) spectra of the nanocrystals before (bottom) and after (top) ligand exchange with dendron ligands. Right panel: transmission electron microscopy (TEM) images of as-synthesized (bottom) and dendron-coated (top; dendron–nanocrystals) Fe_3O_4 nanocrystals. Reprinted with permission from [45], M. Kim et al., *Adv. Mater.* 17, 1429 (2005). © 2005, Wiley-VCH.

unaffected by the change in monolayer composition. Multiple ligands could be readily incorporated into the monolayer using a simultaneous displacement reaction. Rotello and coworkers [48] further developed a facile surface modification method by a ligand exchange reaction using cubic silsesquioxane, anionic octa(tetramethylammonium)polyhedral oligomeric silsesquioxane (TMA–POSS), shown in Figure 18a. A trioctylamine ligand on γ-Fe_2O_3 SPIONs prepared according to the reference method of Rockenberger et al. [12] was successfully exchanged with TMA–POSS via a two-phase reaction. A monolayer exchange using anionic TMA–POSS provides individual particles that are soluble in aqueous environments (Figure 18b) and possesses excellent stability in biologically relevant pH ranges and salt concentrations. Also, this ligand exchange reaction worked well with γ-Fe_2O_3 SPIONs and FePt nanoparticles prepared according to the reference methods of Hyeon et al. [13] and Sun et al. [49], respectively, and proved to be general in nature. Another ligand exchange of surfactant-protected M/Fe_2O_3 (M = Co or $SmCo_{5.2}$) nanoparticles using functionalized diol, dopamine with nitrilotriacetic acid (DA–NTA), was reported [50]. A system with an M/Fe_2O_3–DA–NTA nanostructure was created, as shown in Scheme 3. Upon chelation

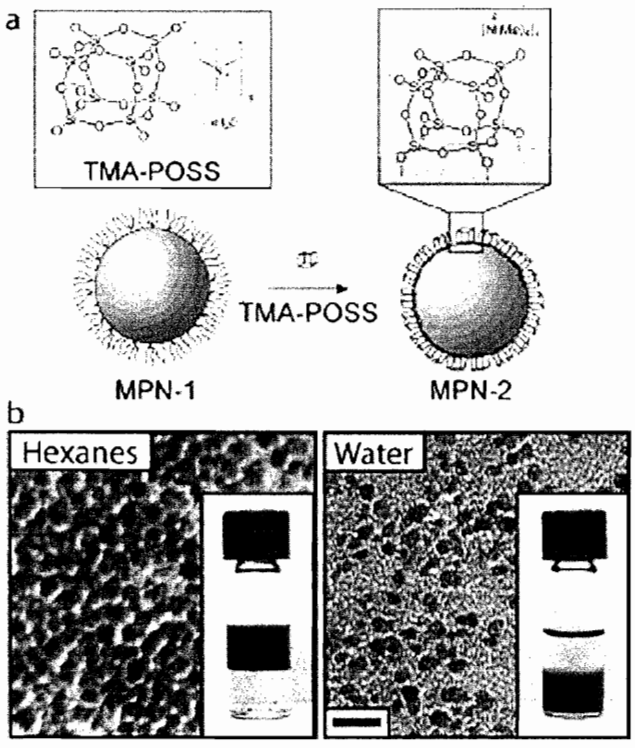

Figure 18. (a) Schematic of passive ligand exchange between hydrophobic monolayer protected nanoparticle (MPN)-1 and anionic octa (tetramethylammonium)polyhedral oligomeric silsesquioxane (TMA-POSS), resulting in water-soluble MPN-2; and (b) transmission electron microscopy (TEM) images of magnetic nanoparticles exchanged with TMA–POSS. Images represent MPN-1 (in hexanes) and MPN-2 (in water), with the inset clearly showing particles transferred from nonpolar to polar solvent after exchange (scale bar = 20 nm). Reprinted with permission from [48], B. L. Frankamp et al., *Chem. Mater.* 18, 956 (2006). © 2006, American Chemical Society.

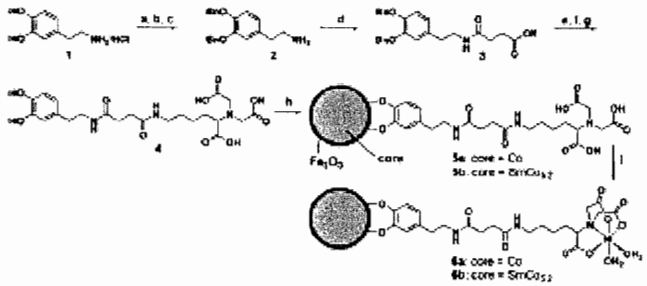

Scheme 3. Conditions: (a) NaOH, *tert*-butyl dicarbonate, dioxane, H_2O, 24 h; (b) BnBr, K_2CO_3, DMF, rt, 24 h; (c) 10% CF_3COOH, CH_2Cl_2, rt, 5 h; (d) succinic anhydride, pyridine, rt, 3 h; (e) NHS, DCC, DMAP, $CHCl_3$, rt, 3 h; (f) $NaHCO_3$, NTA, H_2O, CH_3CH_2COOH, $CHCl_3$, rt, 24 h; HCl; (g) Pd-C, CH_3OH, H_2; (h) hexane-water, sonication for 20 min; and (i) $NiCl_2{\cdot}6H_2O$. Reprinted with permission from [50], C. Xu et al., *J. Am. Chem. Soc.* 126, 9938 (2004). © 2004, American Chemical Society.

to Ni^{2+}, this M/Fe_2O_3–DA–NTA–Ni^{2+} system (**6**) separates histidine-tagged proteins from a cell lysate with high efficiency and capacity. The specificity and efficiency of **6b** remain unaffected even after **6b** is boiled in a buffer solution. The TEM image in Figure 19 indicates that **5a** or **5b** exhibits well-defined core–shell nanostructures similar to the as-prepared Co–Fe_2O_3 or $SmCo_{5.2}$–Fe_2O_3 nanoparticles. Magnetic measurements reveal the superparamagnetic behavior of **6a** and **6b** at 298 K before and after binding to the protein. All the magnetizations are sufficient to allow the magnetic separation of the proteins by a small magnet.

Ligand exchange of surfactant-protected Fe_3O_4 with 2,3-dimercaptosuccinic acid (DMSA) has transformed the SPIONs from hydrophobic to water soluble [51]. The DMSA forms a stable coating through its carboxylic chelate bonding, and further stabilization of the ligand shells is attained through intermolecular disulfide cross-linkages between the ligands under ambient conditions. The remaining free thiol groups of the DMSA ligand are used for the conjugation of organic polymers (here for the conjugation of a targeting antibody, Herceptin). The SPIONs with the DMSA ligand are fairly stable in water and phosphate-buffered saline (PBS) without any aggregation. Their nanoscale size effects on the magnetism and induced magnetic resonance (MR) signals have been examined. The spin–spin relaxation time (*T2*) weighted spin–echo magnetic resonance imaging (MRI) of water-soluble SPIONs shows significant MR image changes from white to black via gray in the size regime from 4 to 12 nm. The general trend is that as water-soluble SPION size increases, the *T2* weighted MR signal intensity continuously decreases and in turn appears as darker MR images. The ligand exchange of surfactant-protected Fe_3O_4 with cationic and anionic ligands provides fairly stable and well-dispersed SPIONs in water [52]. (3-Carboxypropyl)trimethylammonium chloride was ligated to the nanocrystal surface (Scheme 4a). The carboxylate end of the ligand binds to the surface iron, and the appended ammonium cation makes the nanocrystal hydrophilic. In a similar manner, 2-carboxyethyl phosphate was ligated to the nanocrystal surface (Scheme 4b), producing a

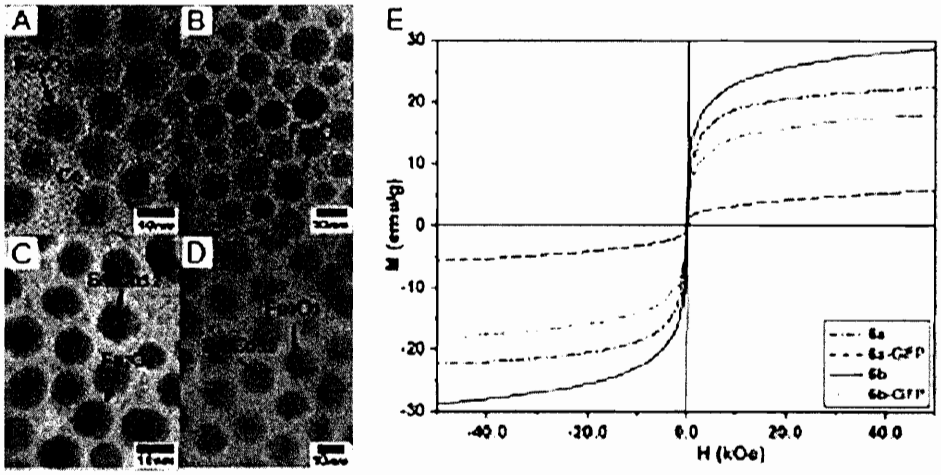

Figure 19. Transmission electron microscopy (TEM) images of (a) Co–Fe_2O_3, (b) **5a**, (c) $SmCo_{5.2}$–Fe_2O_3, and (d) **5b**; and (e) magnetism of **6a**, **6a**-green fluorescent protein (GFP), **6b**, and **6b**-GFP at the ambient conditions. Reprinted with permission from [50], C. Xu et al., *J. Am. Chem. Soc.* 126, 9938 (2004). © 2004, American Chemical Society.

material having anionic phosphonate groups to promote water solubility. TEM analyses of water-soluble SPIONs coated with (3-carboxypropyl)trimethylammonium chloride and with 2-carboxyethyl phosphate show that each retains its individual size without aggregation. The water-soluble SPIONs were tested for a charge-mediated endocytosis. The result matched with the expectation that only cationic water-soluble SPIONs easily anchor to cell membranes through electrostatic interactions and are internalized into cells by way of a charge-mediated endocytosis process.

A liquid-like inorganic SPION core–organic shell has been introduced through surface functionalization by organosilanes [53, 54]. The maghemite SPIONs prepared by coprecipitation were used in this study. The silane solution was added to a suspension of Fe_2O_3 in alkaline water (pH 10), giving the maghemite chloride salt (henceforth described as nanosalts), as shown in Figure 20. When chloride is the counteranion, the nanosalt is isolated in a powder form. No melting is observed even after heating to 150°C, above the surface decomposition temperature of the organic surface modifier. In contrast, replacement of the chloride by $R(OCH_2CH_2)_7O(CH_2)_3$ ions yields a clear liquid at room temperature. The liquid-like nature of the nanosalt was demonstrated by its ability to dissolve the polar dye ethylene blue and nonpolar dye coumarin derivatives. Furthermore, Bourlinos et al. [54] dissolved and polymerized pyrrole to form polypyrrole in the nanosalt medium. Since the superparamagnetism of the nanoparticles remained unaffected through this procedure, a solvent-free, ionically conductive ferrofluid (a "magnetic liquid electrolyte") was obtained. This system showed a liquid-like behavior with only moderate viscosity at room temperature and

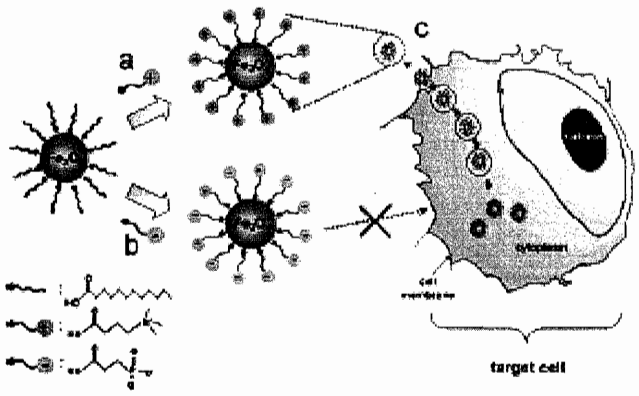

Scheme 4. Schematics of the ligand exchange procedure and utilization in cellular labeling.[a] Reprinted with permission from [52], H.-T. Song et al., *J. Am. Chem. Soc.* 127, 9992 (2005). © 2005, American Chemical Society.

[a]Surface exchange of as-synthesized Fe_3O_4 nanocrystals with either (a) cationic or (b) anionic ligand, and (c) their utilization for cell labeling.

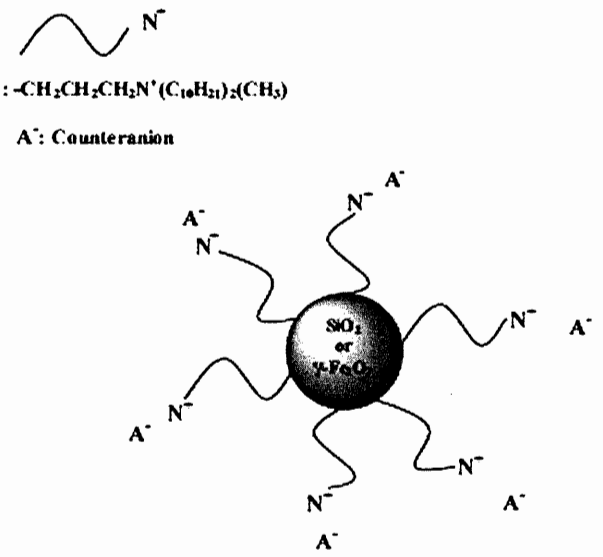

Figure 20. Schematic of the ionically modified nanoparticles. Reprinted with permission from [54], A. B. Bourlinos et al., *Adv. Mater.* 17, 234 (2005). © 2005, Wiley-VCH.

flowed easily at 40°C. This fabrication of "inorganic liquids" represents a new conceptual methodology toward a facile, rational strategy to create inorganic liquids with optimized conductive and rheological properties.

Ligand exchange on oleic acid–coated γ-Fe_2O_3 SPIONs was reported with two types of ligands: (1) phosphonic acid-azid and carboxylic acid–alkyne [55]. The oleic acid was stripped from the particles and exchanged with either the phosphonic acid ligand or 5-hexynoic acid (**1** and **2** in Scheme 5). After washing, the SPIONs were dispersed in chloroform. The newly coated nanoparticles had not formed aggregates. The resultant particles were submitted to copper(I)-catalyzed azid-alkyne cycloaddition (CuAAC) reactions with organic substrates, the products of which were well dispersed in a range of solvents, depending upon the ligand of choice. With **1** and **2**, a CuAAC reaction using the complementary click functional molecule (5-chloropentyne for **1**, and benzyl azid for **2**) was performed to prepare **3** and **4** (Scheme 5). Treatment of **1** with α-acetylene-poly (*tert*-butyl acrylate) (ptBA) polymer (**5**) under CuAAC conditions yielded ptBA-coated particles (**6**), which were well dispersed and for which no aggregation had occurred. All the FTIR spectra after the CuAAC reaction showed the disappearance of the azid peak at 2114 cm^{-1} or the alkyne peak at 2100 cm^{-1}, indicating a high yield for the CuAAC reaction.

Ligand exchange using trialkoxysilane derivatives can be achieved subsequently after stripping the surfactant ligand by treating it with ammonium hydroxide solution [56]. The trialkoxysilane derivatives also can be anchored directly to the SPIONs prepared by the coprecipitation method since these SPIONs have surface hydroxyl groups which are available for Fe–O–Si linkage [57–63]. The other terminus of the trialkoxysilane derivatives can be various, from a small organic group like aminopropyl to an organic polymer such as PEG. Anchoring (3-aminopropyl)-trialkoxysilane (APTRS; R = alkoxy such as methoxy or ethoxy) to the stripped SPION can be followed by covalent conjugation with an activated carboxylic acid group of the next available surface molecule which contains a specific targeting moiety or a biocompatible polymer, which again can be followed by covalent conjugation with a specific targeting molecule. Alternatively, the preconjugated large molecules can be anchored directly to the stripped SPIONs. The representative anchoring and conjugation schemes are shown in Figure 21. A variety of molecules such as MPEG [57, 58], folic acid [57], PEG–folic acid [59, 60], bovine serum albumin (BSA) [61], methotrexate [62], and chlorotoxin [63] have been utilized for amide conjugation to the APTRS-anchored SPION, providing a specific function according to the conjugated molecule. Usually, the anchoring reaction was completed by vortex, sonication, and then incubation of the mixture of SPIONs and silane for 4 h at 60°C. The following amide conjugation reaction was easily accomplished via incubation at 37°C for 4 h with activated carboxyl-containing molecules. The surface-modified SPIONs showed improved intracellular uptake into their specifically targeting cells.

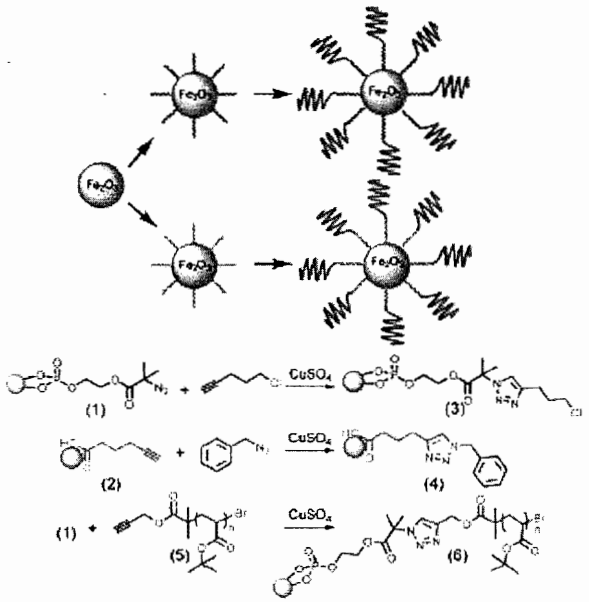

Scheme 5. General scheme for functionalizing the surface of iron oxide nanoparticles. Reprinted with permission from [55], M. A. White et al., *J. Am. Chem. Soc.* 128, 11356 (2006). © 2006, American Chemical Society.

Ligand exchange of oleic acid–coated γ-Fe_2O_3 SPIONs has been accomplished with 3-mercaptopropionic acid (MPA) via an Fe–S covalent bond after the SPIONs were treated with iron pentacarbonyl to make an Fe-rich surface on them [64]. The exchange reaction was straightforward. After the addition of MPA to Fe-rich SPIONs, refluxing for 1 h was enough for ligand exchange. The resultant MPA-anchored SPIONs (SPION–MPAs) turned to be hydrophilic due to the outward-directing carboxylic acid, which was further covalently conjugated to dextran for biocompatibility.

3.1.2. Adsorption of Organic Polymers on SPIONs

The as-synthesized SPIONs or the ligand exchanged or charged SPIONs have been used for the adsorption of organic polymers. Adsorptions of amphiphilic block copolymers [65–69] or in situ polymerizations [70] on the SPIONs have been explored.

Ai et al. [65] used an amphiphilic diblock copolymer of poly(ε-caprolactone)-*b*-poly(ethylene glycol) (PCL-*b*-PEG) for the micelle formation (Figure 22). The PCL segment forms crystalline hydrophobic cores, which lead to stable micelle formation with a very low critical micelle concentration. A cluster of Fe_3O_4 SPIONs prepared according to the reference method of Sun and Zeng [26] was encapsulated inside the hydrophobic core of PCL-*b*-PEG micelles, showing a promising relaxation property as magnetic resonance probes. Their mean hydrodynamic diameters were 75 ± 4, 97 ± 6, and 110 ± 9 nm for the respective 4, 8, and 16 nm SPIONs. Sun and Zeng verified the clustering of SPIONs in the micelle cores by investigating the TEM images (Figure 23). Control of the cluster composite size and of the number of SPION cores encapsulated inside a single-cluster composite has also been reported by Taton and coauthors [66] using 10.9 nm γ-Fe_2O_3 SPIONs prepared by

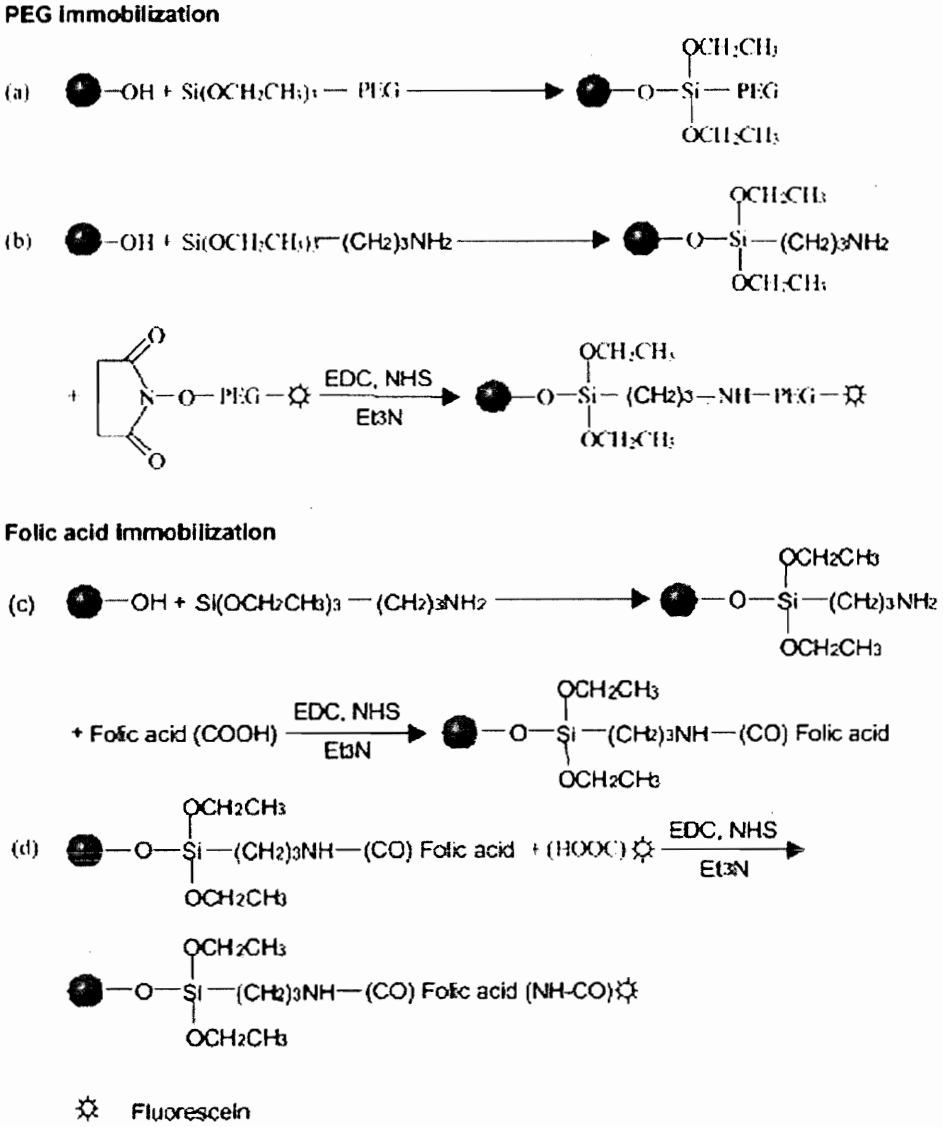

Figure 21. Chemical reaction schemes for immobilizing (a) poly(ethylene glycol) (PEG), (b) PEG–fluorescein, (c) folic acid, and (d) folic acid–fluorescein on the surface of magnetite nanoparticles. Reprinted with permission from [57], Y. Zhang et al., *Biomaterials*, 23, 1553–1561 (2002). © 2002, Elsevier.

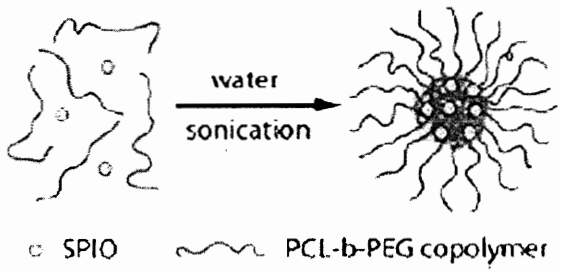

Figure 22. Schematic illustration of superparamagnetic iron oxide (SPIO) micelle formation. Reprinted with permission from [65], H. Ai et al., *Adv. Mater.* 17, 1949 (2005). © 2005, Wiley-VCH.

the reference method of Hyeon et al. [13] and amphiphilic block copolymer poly(styrene$_{250}$-block-acrylic acid$_{13}$) (PS$_{250}$-*b*-PAA$_{13}$). The magnetic properties of the cluster composites were characterized by SQUID magnetometry and followed the general Langevin magnetic model for superparamagnetic materials. Cluster composite suspensions were stable to a variety of biological buffer systems over a wide pH range (pH 2–11). The micellar shells of these cluster composites were functionalized using covalent chemistry that would not ordinarily be possible on the magnetic particle surface. Also, peptide-based copolymers have been used to form polymer micelles or vesicles for encapsulation of both hydrophilic and hydrophobic γ-Fe_2O_3 nanocrystals [67, 68].

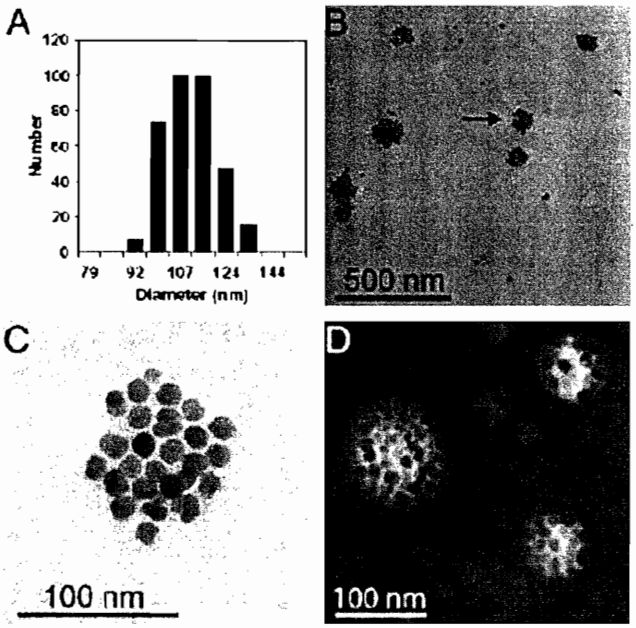

Figure 23. (a) Dynamic light scattering (DLS) histogram showing the size distribution of 16 nm superparamagnetic iron oxide (SPIO)-loaded polymeric micelles based on a poly(ε-caprolactone)-*b*-poly(ethylene glycol) (PCL(5k)-*b*-PEG(5k)) copolymer (mean diameter: 110 nm). (b) Transmission electron microscopy (TEM) of these micelles at low magnification. Isolated clusters of SPIO particles were observed. (c) A high-magnification TEM image of the micelle indicated by the arrow in (b). (d) TEM image of the same micelle sample after negative staining by 2% phosphotungstic acid (PTA). SPIO clusters were found to localize inside the "bright" hydrophobic cores of micelles. Reprinted with permission from [65], H. Ai et al., *Adv. Mater.* 17, 1949 (2005). © 2005, Wiley-VCH.

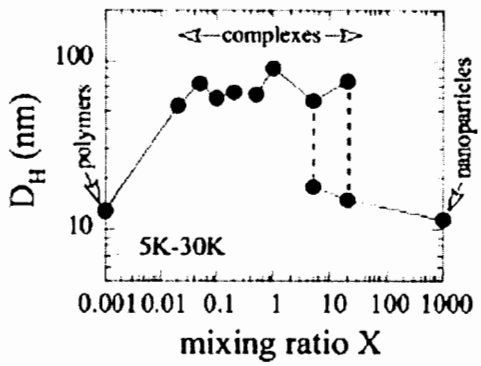

Figure 24. Hydrodynamic diameter D_H as a function of the mixing ratio X for mixed solutions made from poly(trimethylammonium ethylacrylate methyl sulfate)-*b*-poly-(acrylamide) (PTEA(5k)-*b*-PAM(30k)) block copolymers and iron oxide nanoparticles. For large values of X, a second diffusive mode associated to single nanoparticles is indicated. The hydrodynamic diameters D_H for the individual components are $D_H^{pol} = 13$ nm and $D_H^{nano} = 11$ nm. Reprinted with permission from [69], J-F. Berret et al., *J. Am. Chem. Soc.* 128, 1755 (2006). © 2006, American Chemical Society.

When polyelectrolyte-neutral block copolymers are mixed in aqueous solutions with oppositely charged nanoparticles, stable clusters of particles are found to form spontaneously [69]. The mechanism is based on electrostatics and on the compensation between the opposite charges. The cluster of nanoparticles exhibits core–shell microstructure. In the core, the oppositely charged nanoparticles are tightly bound and blocked by the polyelectrolyte, forming a dense coacervate microphase. The shell is made of neutral chains and surrounds the core. Hydrophilic citrate-coated γ-Fe_2O_3 SPIONs prepared by alkaline coprecipitation have negative charges on their surface. Controlled clustering of these SPIONs using polyelectrolyte-neutral block copolymers, poly(trimethylammonium ethylacrylate methyl sulfate)-*b*-poly-(acrylamide) (PTEA(5K)-*b*-PAM(30K)), has been reported [69]. The average hydrodynamic diameter in Figure 24 ranges between 60 and 80 nm for $0.01 < X < 5$, suggesting the formation of mixed polymer-nanoparticle aggregates. The cryo-TEM image in Figure 25 displays mixed aggregates, which are slightly anisotropic with sizes between 20 and 50 nm and involve several tens of nanoparticles.

The superparamagnetic, monodisperse, and charged polystyrene particles containing nanoscale iron oxide nanoparticles were synthesized through emulsion polymerization [70]. Nanoscale iron oxide prepared by the coprecipitation method was treated with oleic acid and sodium dodecyl benzene sulfonate for surface coating. This nanoscale iron oxide solution was used for the emulsion polymerization of styrene, yielding a cluster of SPIONs encapsulated in a polystyrene particle. The resultant superparamagnetic-charged polystyrene particles are monodisperse. They self-assemble into crystalline colloidal arrays (CCAs) in deionized water and Bragg-diffract visible light. The diffraction from these superparamagnetic CCAs can be controlled by the imposition of magnetic fields, which readily alter the CCA lattice constant. The magnetically induced CCA self-assembly can

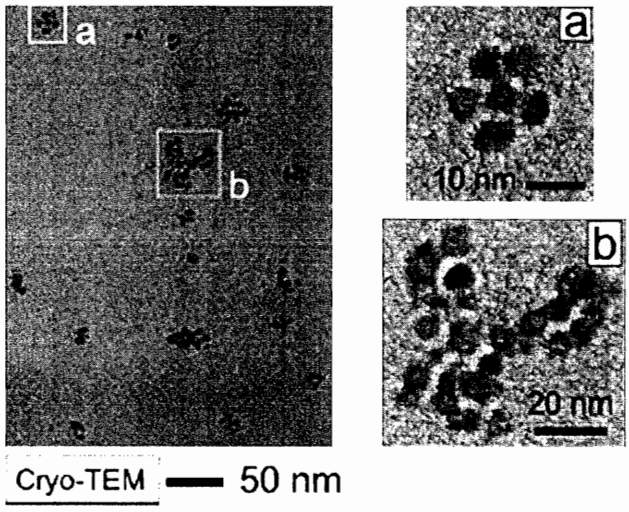

Figure 25. A cryo–transmission electron microscopy (TEM) image of mixed aggregates obtained by complexation of poly(trimethylammonium ethylacrylate methyl sulfate)-*b*-poly-(acrylamide) (PTEA(5k)-*b*-PAM(30k)) and iron oxide nanoparticles. The total concentration is $c = 0.2$ wt. % and $X = X_p$ (= 1). Insets: a zoom of the fields of observation around aggregates **a** and **b** enabled us to discern the densely packed 6.3 nm diameter nanoparticles inside the aggregates. Reprinted with permission from [69], J-F. Berret et al., *J. Am. Chem. Soc.* 128, 1755 (2006). © 2006, American Chemical Society.

be used for the development of potential photonic crystal materials and devices.

Rotello and coauthors [71] showed that interparticle spacing over 2.4 nm could be controlled with increasing dendrimer generation by small-angle X-ray scattering (SAXS) measurement. Cationic SPIONs were prepared by ligand exchange with a cationic long chain 1,3-diol ligand. Treatment of cationic SPIONs with anionic polyamidoamine (PAMAM) dendrimers could produce assemblies featured with systematic interparticle spacing according to the dendrimer generation. The increase in spacing modulated the collective magnetic behavior by effective lowering of the dipolar coupling between particles. The deviation from the predicted dependence of collective behavior on interparticle spacing suggested that a dense assembly of magnetically free particles can exist with a surprisingly small space between particles.

A general method to drastically improve the dispersity of oleic acid–stabilized nanoparticles in aqueous solutions has been reported [72]. Oleic acid–stabilized γ-Fe_2O_3 SPIONs prepared by the reference method of Hyeon et al. [13] formed an inclusion complex between surface-bound surfactant molecules and α-cyclodextrin (α-CD), as shown in Figure 26. The efficiency of the phase transfer to the aqueous solutions depends on the initial α-CD concentration. The nanoparticles stabilized by the α-CD–oleic acid complex can be stable for long periods of time in the aqueous phase under ambient atmospheric conditions.

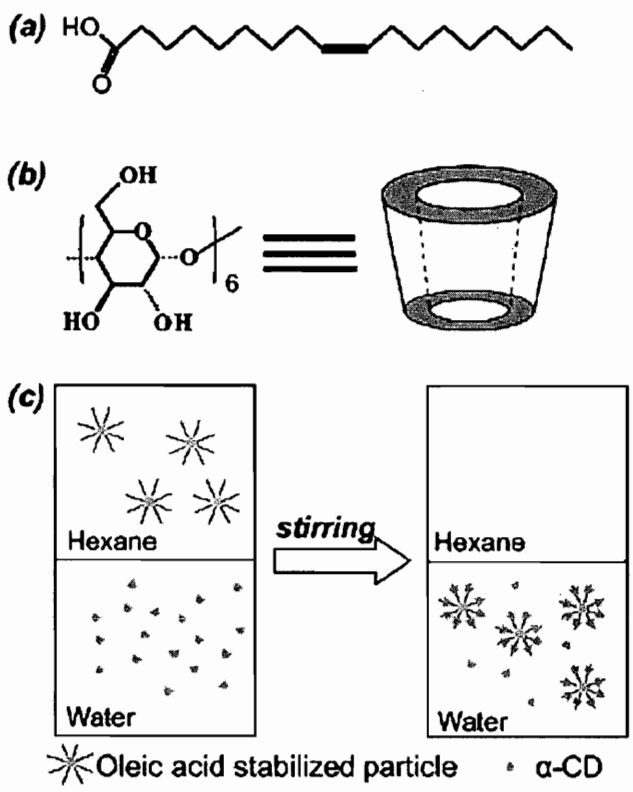

Figure 26. Chemical structures of (a) oleic acid, and (b) α-cyclodextrin (CD) molecules; and (c) a schematic illustration of the transfer of oleic acid–stabilized nanoparticles from the organic into aqueous phase by surface modification using CD. Reprinted with permission from [72], Y. Wang et al., *Nano Lett.* 3, 1555 (2003). © 2003, American Chemical Society.

3.2. Inorganic SPION Core--Inorganic Shell

Silica has been the most frequently used inorganic shell material to encapsulate the SPION core due to its proven biocompatibility and stability in aqueous systems. Moreover, silica chemistry is well-known, and standard chemistry protocols can be followed to conjugate various molecules to the silica surface, thus enabling silica-based particles to couple and label target molecules with selectivity and specificity. The silica coating has been carried via the sol-gel process [73, 74] in aqueous media for the stripped SPIONs [75–79] or in nonpolar organic media for the surfactant-coated SPIONs [80, 81]. Treatment of the SPION solution with tetraethoxysilane (TEOS) and ammonium hydroxide easily produces silica-coated SPIONs with desired shell thickness. Consecutively, further treatment of the resultant solution with aminopropyl silane (APS) provides a SPION–SiO_2 core–shell structure with processable aminopropyl groups. Further surface chemistry after this step has been exploited with a variety of targeting or functioning molecules via amide linkage [57–63, 75–77], and some of them were already reviewed in Section 3.1.1. The representative example is shown in Scheme 6. Silica shell formation always ends up with inclusion of the SPION cluster or multiple SPION cores inside the silica matrix when the stripped SPIONs are used (Figure 27). This seems to occur due to the characteristic chemistry of silica and is well-known even in the core–shell structures of other nanoparticle–silica composites. The SPION–silica core–shell nanostructure containing a single SPION core (Figure 28) has been accomplished by Ying and coauthors [80] via the sol-gel process of reverse micelle–structured SPIONs. After further treatment of SPION–silica composites with APS [81], we found that the resultant SPIONs tend to aggregate probably due to the multiple hydrogen bonds among the terminal NH_2 moieties on the SPIONs. I-methyl-4-(E)-2-{4-[methyl(2-sulfanylethyl)-amino]phenyl}-1-ethenyl) pyridium iodide (ASPI–SH) fluorophore [75] has been attached to the SPION core before silica shell formation, or luminescent pyrene [76] has been included inside the silica shell, providing enhanced contrast magnetic resonance and optical imaging with high stability. A ferromagnetic iron oxide–silica nanocomposite (270 nm) containing a single magnetic core has been prepared by the sol-gel process starting from 120 nm–sized hematite, followed by reduction to an Fe_3O_4–Fe core [82]. The porous silica shell could be produced by utilizing the mixture of TEOS and *n*-octadecyltrimethoxysilane (C_{18}TMS) during the sol-gel process and by calcination [80, 82]. Also, treatment of the SPION–silica nanocomposite with HCl solution could produce a rattle-type SPION–silica nanoball [80].

Xia and coauthors [83] reported a new system based on amorphous selenium (α-Se) which enables the synthesis of monodisperse spherical colloids that exhibit both superparamagnetism and controllable surfaces. Multiple SPION cores were encapsulated in a selenium spherical colloid, further coated with a Pt shell, and then coated again with silica. The α-Se cores can be removed with hydrazine since clinical

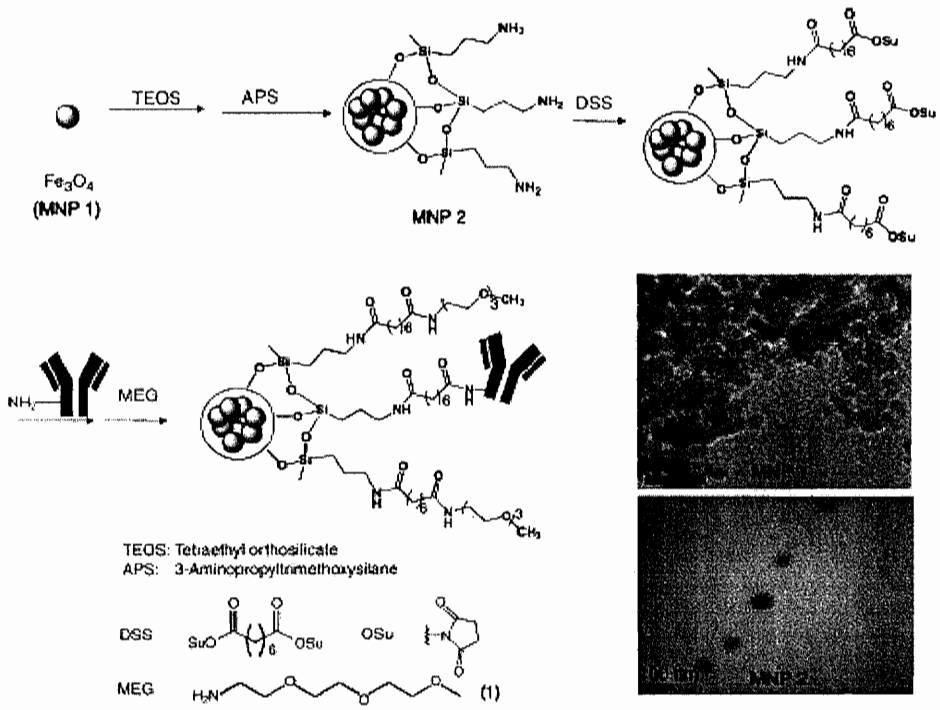

Scheme 6. Preparation and characterization of methoxyethyl-terminated ethylene glycol (MEG)-protected antibody-conjugated magnetic nanoparticles (MNPs). Reprinted with permission from [77], P.-C. Lin et al., *Small* 2, 485 (2006). © 2006, Wiley-VCH.

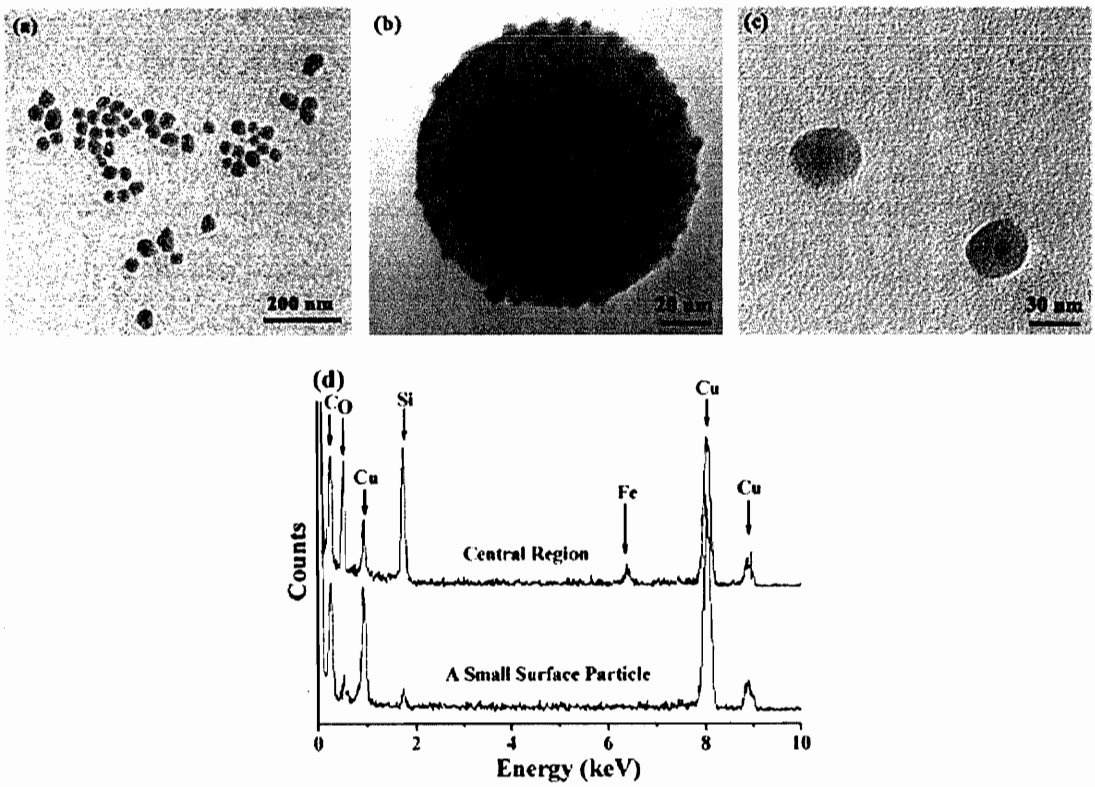

Figure 27. Transmission electron microscopy (TEM) images showing (a) a group of Fe_xO_y–SiO_2 core–shell nanoparticles, and (b, c) Fe_xO_y–SiO_2 core-shell nanoparticles with different surface morphologies. The tetraethyl orthosilicate (TEOS) amount and conditions used for the synthesis of the particles in parts a, b, and c are described in the experimental section of [76]. (d) Energy-dispersive X-ray (EDX) spectra of the central region of a core–shell nanoparticle and a small surface particle. Reprinted with permission from [76], D. Ma et al., *Chem. Mater.* 18, 1920 (2006). © 2006, American Chemical Society.

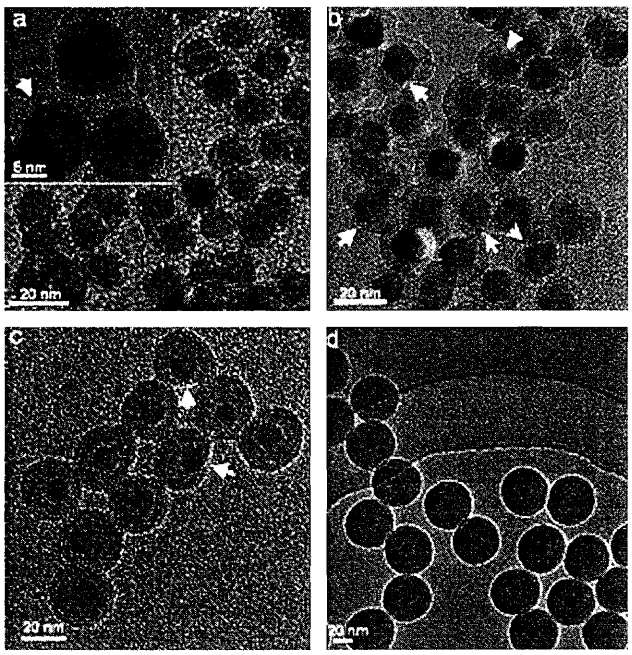

Figure 28. Transmission electron microscopy (TEM) micrographs of Fe_2O_3–SiO_2 nanoparticles with an SiO_2 shell thickness of (a) ~1.8 nm, (b) ~4 nm, (c) ~9 nm, and (d) ~25 nm. Reprinted with permission from [80], D. K. Yi et al., *Chem. Mater.* 18, 614 (2006). © 2006, American Chemical Society.

applications require the magnetic colloids to be nontoxic and stable against sedimentation in the absence of an applied magnetic field. The resultant hollow double-shelled SPION–Pt–silica colloid is expected to be mechanically and chemically stable and superparamagnetic since its interior is loaded with surfactant-coated SPIONs. These magnetic colloids could be used for bioconjugation before and after silica shell formation.

Gold has also been used as an inorganic shell material for the encapsulation of SPIONs [84, 85] since the surface chemistry of the Au nanoparticle is well established. Anchoring a thiolated bifunctional organic molecule onto an Au nanoparticle imparts further chemical reactivity and the opportunity to create multifunctional, reactive nanoparticles. Water-soluble, Au-coated, magnetic iron oxide nanoparticles with diameters of ~60 nm were synthesized by the reduction of Au^{3+} using $HAuCl_4$ onto the surfaces of ~9 nm diameter particles consisting of either γ-Fe_2O_3 or partially oxidized Fe_3O_4 via iterative hydroxylamine seeding [84]. Both starting SPIONs were prepared by coprecipitation under an inert atmosphere, and the former was oxidized in air. The morphology and optical properties of the core–shell particles are dependent on the quantity of deposited Au, while the magnetic properties remain largely independent of Au addition. The Au-coated SPION–Au particles exhibit a surface plasmon resonance peak that blue-shifts from 570 to 525 nm with increasing Au deposition. SQUID magnetometry reveals that particle magnetic properties are not affected by the overlayer of a moderately thick Au shell. The relatively monodisperse SPION–Au core–shell nanocomposite has been prepared starting from relatively monodisperse Fe_3O_4 SPIONs [85]. The Au shell was formed by a combination of thermally activated desorption of the capping layer, deposition of Au using an $Au(OOCCH_3)_3$ precursor on the exposed Fe_3O_4 surface, and subsequent reencapsulation of the Au surface by the capping agent. The TEM images and size distributions of the SPIONs before and after coating with an Au shell are shown in Figure 29. The interfacial reactivity of a combination of ligand exchanging and interparticle cross-linking was exploited for molecularly mediated thin film assemblies of these core–shell nanoparticles.

Instead of making an inorganic shell on SPIONs, Xu and coauthors [86] demonstrated a simple, efficient, and general method to form heterodimeric nanostructures based on the reactions on the colloidosome, as shown in Scheme 7. An organic solution of the as-prepared Fe_3O_4 SPIONs by the reference method of Sun and Zeng [26] was added into an aqueous solution of silver nitrate. Ultrasonic emulsification afforded a stable emulsion of the two solutions. After a 30 min reaction period, centrifugation separated the organic layer, which contained the well-dispersed heterodimers (**1**). The TEM images of the SPION–Ag heterodimers **1** are shown in Figure 30. The authors suggested that two factors prevent the formation of silver shells on the nanoparticles: (1) partial exposure of the nanoparticles to the aqueous phase, and (2) self-catalyzed reduction of the Ag^+ and the nucleation of silver at the partially exposed site. Therefore, the heterodimers with gradually increased Ag spheres should be observed throughout the reduction process. This procedure also allows functional molecules to be attached on specific parts of the heterodimers. The substantial difference in surface chemistry of the two spheres in **1** allows different functional molecules to attach to the heterodimer in a particle-specific way via ligand exchange. For example, compound **4** attached only to Ag, and then, subsequently, compound **5** anchored only to Fe_3O_4. The multifunctional heterodimers such as **7** are hydrophilic, fluorescent, and responsive to magnetic forces, and can bind to specific receptors.

4. APPLICATION

SPIONs have been actively investigated as a colloidal fluid and as a building material of nanostructures for various potential applications.

4.1. Application as a Colloidal Fluid

Surface-modified SPIONs with specific functional moieties have been studied for MR-imaging reagents [51, 52, 60, 63, 65, 87–91], drug and gene delivery [92–94], hyperthermia [95, 96], separation technologies [50, 93, 97], and diagnostic probes [98–101]. The SPION colloidal fluids have also been investigated as catalysts [102, 103].

There are several commercially available SPION–dextran composite particles for MR imaging. For example, Endorem has a rather coarse size distribution of 120–180 nm, and it is extensively used in diagnosis of hepatocellular function [87, 104]. The core materials of these commercial SPION–dextran composites have been prepared by the coprecipitation method and thus show a rather coarse size distribution. The SPIONs have been conjugated to appropriate monoclonal antibodies [88], proteins [89], or peptides [90] to

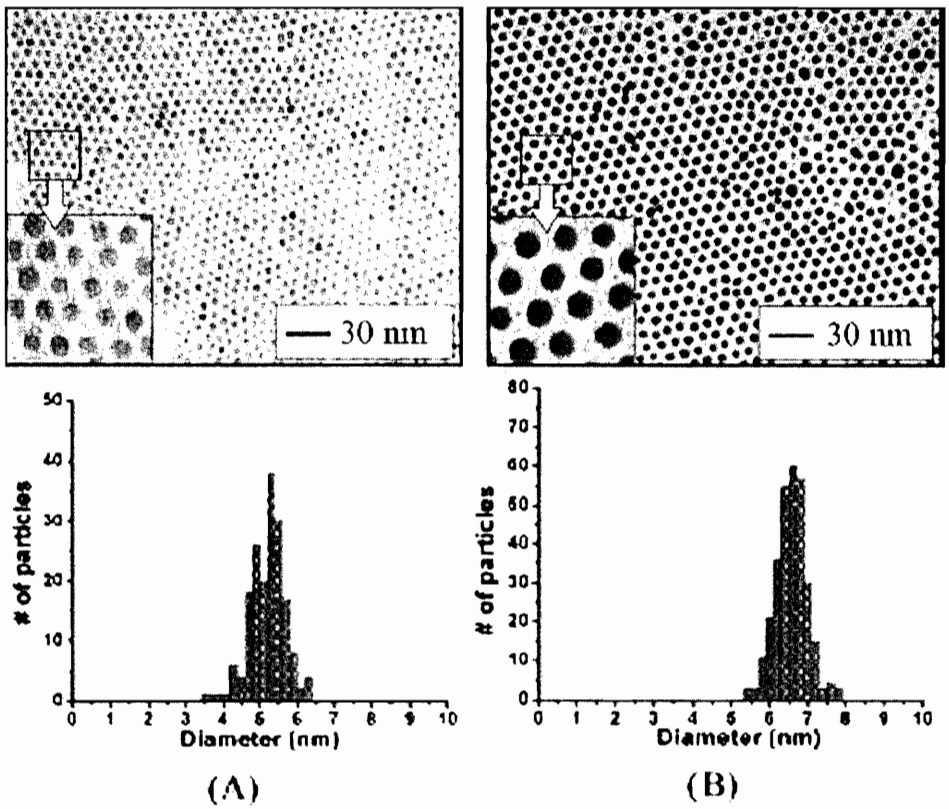

Figure 29. Transmission electron microscopy (TEM) (top panel) micrographs and (bottom panel) size distributions for Fe_3O_4 nanoparticles (a) before and (b) after coating with Au shell. (a) 5.2 ± 0.4 nm; and (b) 6.6 ± 0.4 nm. Reprinted with permission from [85], L. Wang et al., *J. Phys. Chem. B*, 109, 21593 (2005). © 2005, American Chemical Society.

achieve target-directed MRI. For early detection of disease and effective transportation through the extracellular spaces on the order of a few tens of nanometers in the brain, SPION composites of the same size or smaller are required after the functionalization. Using the monodisperse SPIONs

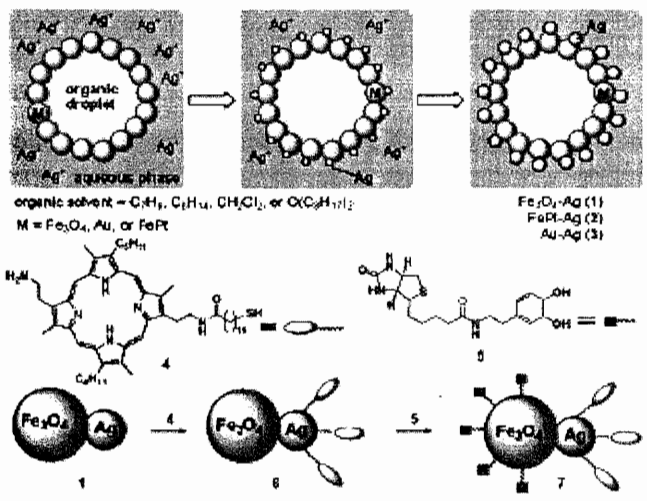

Scheme 7. The synthetic route for making the heterodimers and their surface modificaion. Reprinted with permission from [86], H. Gu et al. *J. Am. Chem. Soc.* 127, 34 (2005). © 2005, American Chemical Society.

with a DMSA ligand, Cheon and coauthors [51] examined the nanoscale size effects on the magnetism and induced MR signals. The *T2*-weighted spin–echo MRI of water-soluble SPIONs shows significant MR image changes from white to black via gray in the size regime from 4 to 12 nm (Figure 31). The general trend is that as water-soluble SPION size increases, the *T2*-weighted MR signal intensity continuously decreases, which in turn appears as darker MR images. These SPIONs with a DMSA ligand were further conjugated to a cancer-targeting antibody, Herceptin, and subsequent utilization of these conjugates as MRI probes demonstrated in vivo selective targeting events of human cancer cells implanted in live mice (Figure 32) [88]. It was also reported that a cluster of monodisperse Fe_3O_4 SPIONs was encapsulated inside the hydrophobic core of PCL-*b*-PEG micelles, showing a promising relaxation property as magnetic resonance probes [65].

Lin and coauthors [92] reported the synthesis of a controlled-release delivery system that is based on MCM-41-type mesoporous silica nanorods (MSNs) capped with SPIONs and is stimuli responsive and chemically inert to guest molecules entrapped in the matrix. After soaking up the guest molecules, the openings of the mesopores of the linker MSN were covalently capped in situ through amidation of the 3-(propyldisulfanyl)propionic acid linker bound at the pore surface with 3-APS-functionalized SPIONs. The disulfide linkages between the MSNs and the SPIONs are

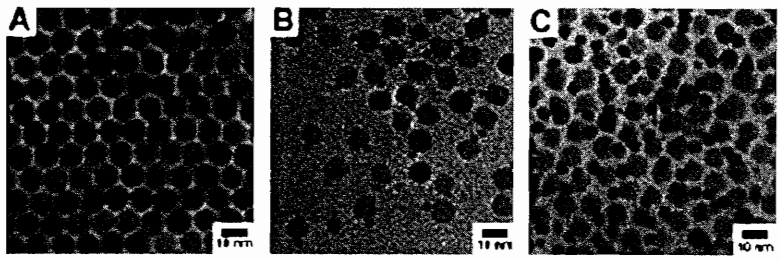

Figure 30. Transmission electron microscopy (TEM) images of (a) the as-prepared Fe_3O_4 nanoparticles; and the Fe_3O_4–Ag heterodimers (b) after a 10 min reaction, and (c) after the reaction stopped at 30 min. Reprinted with permission from [86], H. Gu et al., *J. Am. Chem. Soc.* 127, 34 (2005). © 2005, American Chemical Society.

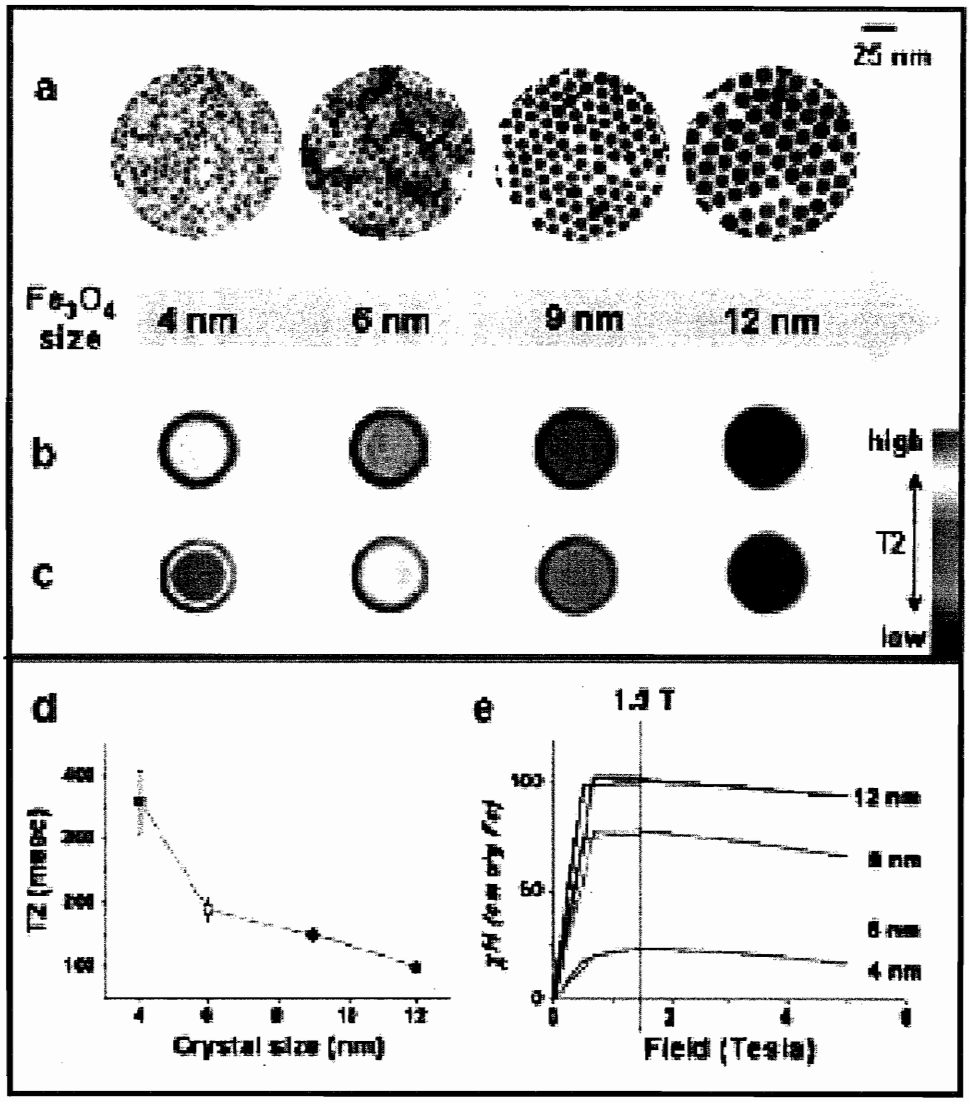

Figure 31. Nanoscale size effect of water-soluble iron oxide (WSIO) nanocrystals on magnetism and induced magnetic resonance (MR) signals. (a) Transmission electron microscopy (TEM) images of Fe_3O_4 nanocrystals of 4 to 6, 9, and 12 nm. (b) Size-dependent *T2*-weighted MR images of WSIO nanocrystals in aqueous solution at 1.5 T. (c) Size-dependent changes from red to blue in color-coded MR images based on *T2* values. (d) Graph of *T2* value versus WSIO nanocrystal size. (e) Magnetization of WSIO nanocrystals measured by a superconducting quantum interference device (SQUID) magnetometer. Reprinted with permission from [51], Y.-W. Jun et al., *J. Am. Chem. Soc.* 127, 5732 (2005). © 2005, American Chemical Society.

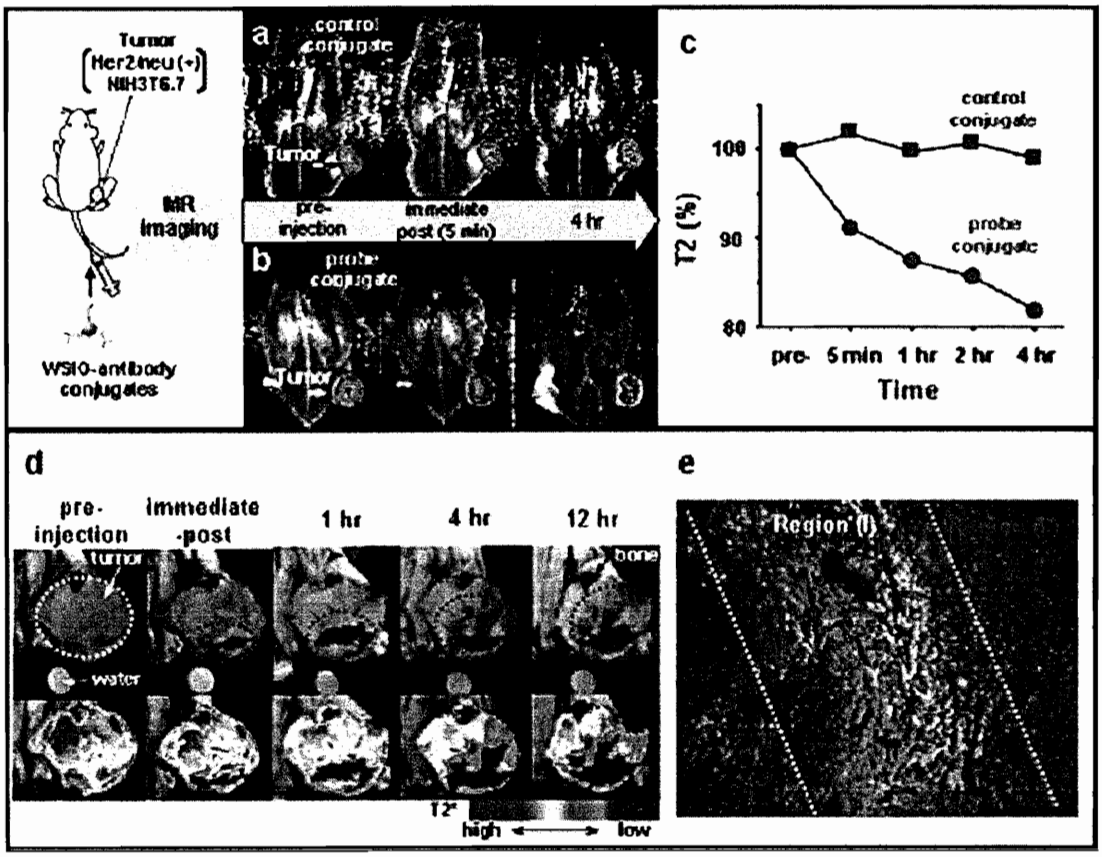

Figure 32. In vivo magnetic resonance imaging (MRI) of cancer-targeting events of water-soluble iron oxide (WSIO)-antibody conjugates. (a, b) Color maps of *T2*-weighted magnetic resonance (MR) images of cancer cell–implanted (NIH3T6.7) mice at the different temporal points (preinjection, immediate postinjection, and 4 h) after the intravenous injection of (a) WSIO-irrelevant antibody control conjugates, and (b) WSIO-Herceptin probe conjugates. Whereas no difference is seen in the color-mapped MRI for the control conjugate (a), an immediate (5 min) color change to blue at the tumor site is evident with the probe conjugate (b). (c) Plot of *T2* values versus time after the injection of WSIO-antibody conjugates in (a) and (b) samples. (d) $T2^*$-weighted MR images of cancer cell-implanted (NIH3T6.7) mouse at 9.4 T and their color maps at different temporal points after probe conjugate injection. The tumor area is circled with white dotted lines. A dark MR image (red dotted circle) immediately appears near the bottom region of the tumor and then gradually diffuses to the central and upper region of the tumor. Color mapping of the identical MR images shows more details of MR signal changes. Progressive diffusion and targeting events of the probe conjugates (blue and green color) into tumor tissue are clearly observed, with their increased occupation of roughly one-third, one-half, and two-thirds of tumor tissues at 1, 4, and 12 h, respectively. (e) Fluorescence immunohistochemical analyses of an excised tumor slice. Endothelial vessels were stained with rhodamine-anti-CD31 (red fluorescence), and probe conjugates were stained with fluorescein isothiocyanate (FITC)-anti-human IgG (green fluorescence). These fluorescence data indicate the presence of WSIO-Herceptin probe conjugates near the highly vascular region I of the tumor tissue. Blue background fluorescence (cell nuclei stained with 4',6-diamidino-2-phenylindole (DAPI) is observed at low vascular region II. Reprinted with permission from [88], Y-M. Huh et al., *J. Am. Chem. Soc.* 127, 12387 (2005). © 2005, American Chemical Society.

chemically labile and can be cleaved with various cell-produced antioxidants and disulfide-reducing agents such as dihydrolipoic acid (DHLA) and dithiothreitol (DTT), respectively. The release of the magnetic nanoparticle caps from the guest-loaded MSNs can be regulated by the concentration of trigger molecules. The synthesis of magnetic nanotubes (MNTs) using porous alumina film as a template and their uses for magnetic-field-assisted chemical and biochemical separations, immunobinding, and drug delivery have been described [93].

The SPIONs dispersed in a polymer matrix have been coated with target-specific molecules and studied for their diagnostic purposes in magnetoresistive DNA chips or biosensors [98–100]. Also, composite particles with the optical and chemical properties of DNA-functionalized gold nanoparticles and the superparamagnetic properties of Fe_3O_4 nanoparticles have been introduced [101]. These structures exhibited the highly cooperative binding property that is key to highly selective biodiagnostic systems based upon nanoparticle probes.

4.2. Application as a Building Material for Nanostructure Construction

Advances in synthesizing SPIONs have enabled precise control over their composition, size, shape, crystal structure, and surface chemistry, as has been reviewed in the previous sections. The distinct properties of the nanoparticle building blocks can be harnessed in assemblies with new collective properties for many potential applications, such as

ultra-high-density magnetic storage media, magnetooptical devices, and biosensors. Nanostructure buildup with SPIONs has been studied for one-dimensional (1D) self-assembly [105], two-dimensional (2D) and three-dimensional (3D) self-assembly [27, 71, 106–109], patterned arrays [110, 111], and covalently linked arrays [112] onto the substrate.

Minko and coauthors [105] reported the fabrication of wirelike 1D structures made by linking Fe_3O_4 SPIONs with polyelectrolyte polymers under a magnetic field. The original SPION particles are stabilized by citric acid, and their surface is negatively charged in aqueous solutions. The positively charged polyelectrolyte poly(2-vinyl N-methylpyridinium iodide) was used to stabilize the wires via the formation of a polyelectrolyte complex. Slow injection of a SPION solution with a pipette on the bottom of the cell containing polyelectrolyte polymer solution produced 1D nanowires. The magnetic nanowires could be manipulated in an external magnetic field and used as building blocks for the fabrication of hierarchical 2D and 3D structures. Redl et al. [106] reported the self-assembly of PbSe semiconductor quantum dots and Fe_2O_3 SPIONs into precisely ordered 3D superlattices. The use of specific size ratios directed the assembly of the magnetic and semiconducting nanoparticles into AB_{13} or AB_2 superlattices with potentially tunable optical and magnetic properties. It was suggested that this synthesis concept could ultimately enable the fine-tuning of material responses to magnetic, electrical, optical, and mechanical stimuli. Also, highly ordered 2D monolayer and 3D superlattice structures of the Fe_3O_4 SPIONs with a large area have been obtained depending on the concentration [107]. An ordered 2D array of Fe_2O_3 particles has been utilized as a template for the fabrication of highly ordered anodic porous alumina with holes less than 10 nm [108]. Oleic acid-ligated Fe_3O_4 SPION spheres have been self-assembled on exfoliated perovskite 3-aminopropylsilylated $[H_{1-x}Ca_2Nb_3O_{10}]^{x-}$ colloidal sheets [109]. The bonding in the aggregates was explained to involve both van der Waals and covalent interactions between NH_2 groups and Fe_3O_4 particles because nonaminated perovskite sheets also exhibit a weak affinity to oleic acid–ligated Fe_3O_4 particles. Interestingly, dilute dispersions of the composite are opalescent due to light reflection, scattering, and absorption by randomly oriented nano- and microparticles. In a magnetic field, the anisotropic aggregates adopt a preferential orientation, and refractive index and light-scattering properties assume a directional dependence, that is, the suspension becomes birefringent, as demonstrated in Figure 33.

Arrays of coprecipitated Fe_3O_4 nanoparticles have been patterned via dip-pen nanolithography (DPN), with precise size control [110]. DPN allows one to transport molecules to a surface, much like a macroscopic dip pen transfers ink to paper, but with the resolution of a conventional atomic force microscope (AFM). Chemisorption of an ink (e.g., 16-mercaptohexadecanoic acid) onto the Au substrate leads to stable nanostructures, which can subsequently be used as templates to assemble SPIONs. Patterned Langmuir-Blodgett films of monodisperse γ-Fe_2O_3 SPIONs have been transferred onto solid substrates such as silicon wafers or poly(dimethylsiloxane) (PDMS) stamps using soft lithography

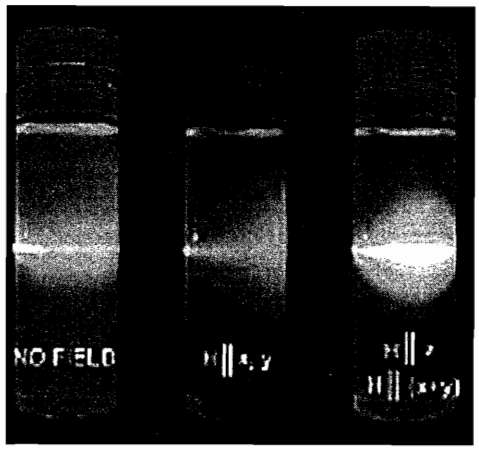

Figure 33. Propagation of laser light (500–550 nm) through a dilute suspension of $(Bu_4N)_x[H_{1-x}Ca_2Nb_3O_{10}\text{-}NH_2]\cdot[Fe_3O_4\text{–}OA]$ in tetrahydrofuran (THF) in the absence and presence of magnetic fields (1000 Oe) with the indicated orientations. Reprinted with permission from [109], F. E. Osterloh et al., *J. Am. Chem. Soc.* 124, 6248 (2002). © 2002, American Chemical Society.

[111]. The Langmuir film was compressed into close-packed domains with diminishing void spaces at increasing surface pressure up to ~65 mN/m. Using the PDMS stamp of microdot patterns (μ dots, 1.0–1.5 μm in diameter), double layers of monodisperse γ-Fe_2O_3 SPIONs were transferred onto a silicon wafer. Figure 34a is a field emission scanning electron microscopy (FESEM) image of the μ-dot-patterned film of γ-Fe_2O_3 SPIONs on a piece of silicon wafer. The quality of the original photo master (Figure 34b), the replicated PDMS stamps, and the applied pressure are some of the key factors that can affect the shapes of the printed μ dots of γ-Fe_2O_3 SPIONs.

A new method has been described to prepare a homogeneous monolayer of ω-alk-1-ene-silane-functionalized Fe_3O_4 SPIONs covalently linked to a hydrogen-terminated silicon (111) surface by a thermal hydrosilylation reaction [112]. The ω-alk-1-ene-silane-functionalized Fe_3O_4 SPIONs were obtained by a monolayer exchange reaction based on the incorporation of trimethoxy-7-octen-1-yl-silane into the oleic acid coating. This type of ligand exchange reaction has been reviewed in Section 3.1.1.

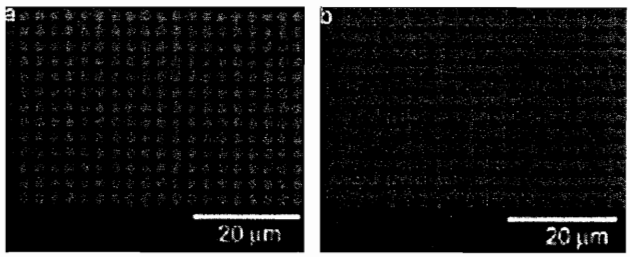

Figure 34. Scanning electron microscopy (SEM) images of (a) patterned μ-dot arrays of γ-Fe_2O_3 nanoparticle Langmuir-Blodgett (LB) film on a silicon wafer, and (b) the original photoresist pattern of μ dots. Reprinted with permission from [111], Q. Guo et al., *J. Am. Chem. Soc.* 125, 630 (2003). © 2003, American Chemical Society.

5. CONCLUSION

This review chapter shows how SPIONs can be prepared and characterized, how their surfaces can be modified for the endowment of a specific function, and how they can be investigated for potential technological applications. Surface-modified SPION colloidal fluids have a variety of applications such as MR imaging reagents, drug and gene delivery, hyperthermia, separation technologies, diagnostic probes, sensors, and catalysts. They also can be used as building blocks for nanostructure construction for potential applications in the fields of ultra-high-density magnetic storage media and magnetooptical devices.

The establishment of preparation and characterization methods of monodisperse SPIONs has accelerated the emergence of surface modification chemistry and nanostructure construction, which are the most actively pursued research areas now. However, the practical application of modified SPION colloids is still in its childhood, though some classical SPION core–polymer shell composites are commercially available. Exciting and important developments can be expected in the near future by bringing together new techniques and interdisciplinary research into high-quality SPIONs. Though the combination of techniques and nanostructures presented here with biomolecules is intensively studied, those involving molecular electronics, nanotubes, and semiconductor quantum dots are almost unexplored and yet hold enormous possibilities for nanotechnology applications. Novel magnetically functional nanocolloids and nanostructures are likely to find fruitful practical applications in the near future.

ACKNOWLEDGMENTS

The author expresses thanks for financial support from the Korean Ministry of Science and Technology through Grant No. 2006-03155 of the Nano R&D Program and Future Key Technology Program.

REFERENCES

1. R. M. Cornell and U. Schwertmann, "The Iron Oxides," Weinheim, Germany: Wiley-VCH, 2003.
2. D. Jiles, "Introduction to Magnetism and Magnetic Materials," London: Chapman & Hall, 1998.
3. U. Häfeli, W. Schütt, J. Teller, and M. Zborowski, "Scientific and Clinical Applications of Magnetic Carriers" (U. Häfeli, W. Schütt, J. Teller, and M. Zborowski, Eds.), New York: Plenum Press, 1997.
4. J. Z. Jiang, R. Lin, W. Lin, K. Nielsen, S. Mørup, K. Dam-Johansen, and R. Clasen, *J. Phys. D* 30, 1459 (1997).
5. M. Benz, A. M. van der Kraan, and R. Prins, *J. Appl. Catal. A* 172, 149 (1998).
6. A. S. Lubbe, C. Bergemann, F. Brock, and D. G. McClure, *J. Magn. Magn. Mater.* 194, 149 (1999).
7. D. Pouliquen, H. Perroud, F. Calza, P. Jallet, and J. Lejeune, *Magn. Reson. Med.* 24, 75 (1992).
8. F. X. Redl, C. T. Black, G. C. Papaefthymiou, R. L. Sandstrom, M. Yin, H. Zeng, C. B. Murray, and S. P. O'Brien, *J. Am. Chem. Soc.* 126, 14583 (2004).
9. K. Woo and H. J. Lee, *J. Magn. Magn. Mater.* 272–276, e1155 (2004).
10. F. Bødker, M. F. Hansen, C. B. Koch, K. Lefmann, and S. Mørup, *Phys. Rev. B* 61, 6826 (2000).
11. R. Zboril, M. Mashlan, and D. Petridis, *Chem. Mater.* 14, 969 (2002).
12. J. Rockenberger, E. C. Scher, and A. P. Alivisatos, *J. Am. Chem. Soc.* 121, 11595 (1999).
13. T. Hyeon, S. S. Lee, J. Park, Y. Chung, and H. B. Na, *J. Am. Chem. Soc.* 123, 12798 (2001).
14. T. Hyeon, *Chem. Commun.* 927 (2003).
15. K. Woo, J. Hong, S. Choi, H.-W. Lee, J.-P. Ahn, C. S. Kim, and S. W. Lee, *Chem. Mater.* 16, 2814 (2004).
16. J. Park, E. Lee, N.-M. Hwang, M. Kang, S. C. Kim, Y. Hwang, J.-G. Park, H.-J. Noh, J.-Y. Kim, J.-H. Park, and T. Hyeon, *Angew. Chem. Int. Ed.* 44, 2872 (2005).
17. J. Park, K. An, Y. Hwang, J.-G. Park, H.-J. Noh, J.-Y. Kim, J.-H. Park, N.-M. Hwang, and T. Hyeon, *Nat. Mater.* 3, 891 (2004).
18. J. Cheon, N.-J. Kang, S.-M. Lee, J.-H. Lee, J.-H. Yoon, and S. J. Oh, *J. Am. Chem. Soc.* 126, 1950 (2004).
19. X. Teng and H. Yang, *J. Mater. Chem.* 14, 774 (2004).
20. M. Casula, Y.-W. Jun, D. J. Zaziski, E. M. Chan, A. Corrias, and A. P. Alivisatos, *J. Am. Chem. Soc.* 128, 1675 (2006).
21. S. Peng, C. Wang, J. Xie, and S. Sun, *J. Am. Chem. Soc.* 128, 10676 (2006).
22. S. Yu and G. M. Chow, *J. Nanosci. Nanotechnol.* 6, 2135 (2006).
23. J. Lai, K. V. P. M. Shafi, A. Ulman, K. Loos, R. Popovitz-Biro, Y. Lee, T. Yogt, and C. Estournes, *J. Am. Chem. Soc.* 127, 5730 (2005).
24. A. L. Willis, N. J. Turro, and S. O'Brien, *Chem. Mater.* 17, 5970 (2005).
25. M. W. A. Yin, F. Redl, N. J. Turro, and S. P. O'Brien, *J. Mater. Res.* 19, 1208 (2004).
26. S. Sun and H. Zeng, *J. Am. Chem. Soc.* 124, 8204 (2002).
27. K. Parvin, J. Ma, J. Ly. X. C. Sun, D. E. Nikles, K. Sun, and L. M. Wang, *J. Appl. Phys.* 95, 7121 (2004).
28. S. Sun, H. Zeng, D. B. Robinson, S. Raoux, P. M. Rice, S. X. Wang, and G. Li, *J. Am. Chem. Soc.* 126, 273 (2004).
29. J. Xie, S. Peng, N. Brower, N. Pourmand, S. X. Wang, and S. Sun, *Pure Appl. Chem.* 78, 1003 (2006).
30. Z. Li, L. Wei, M. Gao, and H. Lei, *Adv. Mater.* 17, 1001 (2005).
31. C.-R. Lin, R.-K. Chiang, J.-S. Wang, and T.-W. Sung, *J. Appl. Phys.* 99, 08N710 (2006).
32. A. B. Bourlinos, A. Bakandritsos, V. Georgakilas, V. Tzitzios, and D. Petridis, *J. Mater. Sci.* 41, 5250 (2006).
33. K. Woo, H. J. Lee, J.-P. Ahn, and Y. S. Park, *Adv. Mater.* 15, 1761 (2003).
34. K. Woo and H. J. Lee, *Key Eng. Mater.* 277–279, 876 (2005).
35. Y. S. Kang, S. Risbud, J. F. Rabolt, and P. Stroeve, *Chem. Mater.* 8, 2209 (1996).
36. C.-Y. Hong, I. J. Jang, H. E. Horng, C. J. Hsu, Y. D. Yao, and H. C. Yang, *J. Appl. Phys.* 81, 4275 (1997).
37. T. Fried, G. Shemer, and G. Markovich, *Adv. Mater.* 13, 1158 (2001).
38. D. K. Kim, Y. Zhang, W. Voit, K. V. Rao, and M. Muhammed, *J. Magn. Magn. Mater.* 225, 30 (2001).
39. O. Perales-Perez, H. Sasaki, A. Kasuya, B. Jeyadevan, K. Tohji, T. Hihara, and K. Sumiyama, *J. Appl. Phys.* 91, 6958 (2002).
40. S. Liu, X. Wei, M. Chu, J. Peng, and Y. Xu, *Coll. Surf. B: Biointerfaces* 51, 101 (2006).
41. D. K. Kim, M. Mikhaylova, F. H. Wang, J. Kehr, B. Bjelke, Y. Zhang, T. Tsakalakos, and M. Muhammed, *Chem. Mater.* 15, 4343 (2003).
42. S. Si, C. Li, X. Wang, D. Yu, Q. Peng, and Y. Li, *Cryst. Growth Des.* 5, 391 (2005).
43. Z. Liu, D. Zhang, S. Han, C. Li, B. Lei, W. Lu, J. Fang, and C. Zhou, *J. Am. Chem. Soc.* 127, 6 (2005).
44. C.-J. Jia, L.-D. Sun, Z.-G. Yan, L.-P. You, F. Luo, X.-D. Han, Y.-C. Pang, Z. Zhang, and C.-H. Yan, *Angew. Chem. Int. Ed.* 44, 4328 (2005).
45. M. Kim, Y. Chen, Y. Liu, and X. Peng, *Adv. Mater.* 17, 1429 (2005).
46. J. P. Folkers, C. B. Gorman, P. E. Laibinis, S. Buchholz, G. M. Whitesides, and R. G. Nuzzo, *Langmuir* 11, 813 (1995).

47. A. K. Boal, K. Das, M. Gray, and V. M. Rotello, *Chem. Mater.* 14, 2628 (2002).
48. B. L. Frankamp, N. O. Fischer, R. Hong, S. Srivastava, and V. M. Rotello, *Chem. Mater.* 18, 956 (2006).
49. S. Sun, C. Murray, D. Weller, L. Folks, and A. Moser, *Science* 287, 1989 (2000).
50. C. Xu, K. Xu, H. Gu, R. Zheng, H. Liu, X. Zhang, Z. Guo, and B. Xu, *J. Am. Chem. Soc.* 126, 9938 (2004).
51. Y.-W. Jun, Y.-M. Huh, J.-S. Choi, J.-H. Lee, H.-T. Song, S. Kim, S. Yoon, K.-S. Kim, J. S. Shin, J.-S. Suh, and J. Cheon, *J. Am. Chem. Soc.* 127, 5732 (2005).
52. H.-T. Song, J.-S. Choi, Y.-M. Huh, S. Kim, Y.-W. Jun, J.-S. Suh, and J. Cheon, *J. Am. Chem. Soc.* 127, 9992 (2005).
53. B. Smarsly and H. Kaper, *Angew. Chem. Int. Ed.* 44, 3809 (2005).
54. A. B. Bourlinos, R. Herrera, N. Chalkias, D. D. Jiang, Q. Zhang, L. A. Archer, and E. P. Giannelis, *Adv. Mater.* 17, 234 (2005).
55. M. A. White, J. A. Johnson, J. T. Koberstein, and N. J. Turro, *J. Am. Chem. Soc.* 128, 11356 (2006).
56. N. Kohler, G. E. Fryxell, and M. Zhang, *J. Am. Chem. Soc.* 126, 7206, (2004).
57. Y. Zhang, N. Kohler, and M. Zhang, *Biomaterials* 23, 1553 (2002).
58. D. K. Kim, M. Mikhaylova, Y. Zhang, and M. Muhammed, *Chem. Mater.* 15, 1617 (2003).
59. Y. Zhang, C. Sun, N. Kohler, and M. Zhang, *Biomed. Microdev.*, 6:1, 33 (2004).
60. C. Sun, R. Sze, and M. Zhang, *J. Biomed. Mater. Res. A*, 550 (2006).
61. M. Mikhaylova, D. K. Kim, C. C. Berry, A. Zagorodni, M. Toprak, A. S. G. Curtis, and M. Muhammed, *Chem. Mater.* 16, 2344 (2004).
62. N. Kohler, C. Sun, J. Wang, and M. Zhang, *Langmuir* 21, 8858 (2005).
63. O. Veiseh, C. Sun, J. Gunn, N. Kohler, P. Gabikian, D. Lee, N. Bhattarai, R. Ellenbogen, R. Sze, A. Hallahan, J. Olson, and M. Zhang, *Nano Lett.* 5, 1003 (2005).
64. K. Woo and J. Hong, *IEEE Trans. Magn.* 41, 4137 (2005).
65. H. Ai, C. Flask, B. Weinberg, X. Shuai, M. D. Pagel, D. Farrell, J. Duerk, and J. Gao, *Adv. Mater.* 17, 1949 (2005).
66. B.-S. Kim, J.-M. Qiu, J.-P. Wang, and T. A. Taton, *Nano Lett.* 5, 1987 (2005).
67. L. E. Euliss, S. G. Grancharov, S. O'Brien, T. J. Deming, G. D. Stucky, C. B. Murray, and G. A. Held, *Nano Lett.* 3, 1489 (2003).
68. S. Lecommandoux, O. Sandre, F. Checot, J. Rodriguez-Hernandez, and R. Perzynski, *Adv. Mater.* 17, 712 (2005).
69. J.-F. Berret, N. Schonbeck, F. Gazeau, D. E. Kharrat, O. Sandre, A. Vacher, and M. Airiau, *J. Am. Chem. Soc.* 128, 1755 (2006).
70. X. Xu, G. Friedman, K. D. Humfeld, S. A. Majetich, and S. A. Asher, *Chem. Mater.* 14, 1249 (2002).
71. B. L. Frankamp, A. K. Boal, M. T. Tuominen, and V. M. Rotello, *J. Am. Chem. Soc.* 127, 9731 (2005).
72. Y. Wang, J. F. Wong, X. Teng, X. Z. Lin, and H. Yang, *Nano Lett.* 3, 1555 (2003).
73. W. Stöber and A. Fink, *J. Coll. Interf. Sci.* 26, 62 (1968).
74. Y. Lu, Y. Yin, B. T. Mayers, and Y. Xia, *Nano Lett.* 2, 183 (2002).
75. L. Levy, Y. Sahoo, K.-S. Kim, E. J. Bergey, and P. N. Prasad, *Chem. Mater.* 14, 3715 (2002).
76. D. Ma, J. Guan, F. Normandin, S. Denommee, G. Enright, T. Veres, and B. Simard, *Chem. Mater.* 18, 1920 (2006).
77. P.-C. Lin, P.-H. Chou, S.-H. Chen, H.-K. Liao, K.-Y. Wang, Y.-J. Chen, and C.-C. Lin, *Small*, 2, 485 (2006).
78. Y. Sun, L. Duan, Z. Guo, Y. DuanMu, M. Ma, L. Xu, Y. Zhang, and N. Gu, *J. Magn. Magn. Mater.* 285, 65 (2005).
79. P. Tartaj, T. González-Carreño, and C. J. Serna, *Adv. Mater.* 13, 1620 (2001).
80. D. K. Yi, S. S. Lee, G. C. Papaefthymiou, and J. Y. Ying, *Chem. Mater.* 18, 614 (2006).
81. K. Woo, J. Hong, and J.-P. Ahn, *J. Magn. Magn. Mater.* 293, 177 (2005).
82. W. Zhao, J. Gu, L. Zhang, H. Chen, and J. Shi, *J. Am. Chem. Soc.* 127, 8916 (2005).
83. U. Jeong, T. Herricks, E. Shahar, and Y. Xia, *J. Am. Chem. Soc.* 127, 1098 (2005).
84. J. L. Lyon, D. A. Fleming, M. B. Stone, P. Schiffer, and M. E. Williams, *Nano Lett.* 4, 719 (2004).
85. L. Wang, J. Luo, Q. Fan, M. Suzuki, I. S. Suzuki, M. H. Engelhard, Y. Lin, N. Kim, J. Q. Wang, and C.-J. Zhong, *J. Phys. Chem. B*, 109, 21593 (2005).
86. H. Gu, Z. Yang, J. Gao, C. K. Chang, and B. Xu, *J. Am. Chem. Soc.* 127, 34 (2005).
87. D. K. Kim, Y. Zhang, J. Kehr, T. Klason, B. Bjelke, and M. Muhammed, *J. Magn. Magn. Mater.* 225, 256 (2001).
88. Y.-M. Huh, Y.-W. Jun, H.-T. Song, S. Kim, J.-S. Choi, J.-H. Lee, S. Yoon, K.-S. Kim, J.-S. Shin, J.-S. Suh, and J. Cheon, *J. Am. Chem. Soc.* 127, 12387 (2005).
89. E. A. Schellenberger, D. Sosnovik, R. Weissleder, and L. Josephson, *Bioconj. Chem.* 15, 1062 (2004).
90. O. A. Garden, P. R. Reynolds, J. Yates, D. J. Larkman, F. M. Marelli-Berg, D. O. Haskard, A. D. Edwards, and A. J. T. George, *J. Immunol. Met.* 314, 123 (2006).
91. A. S. Arbab, W. Liu, and J. A. Frank, *Exp. Rev. Med. Dev.* 3, 427 (2006).
92. S. Giri, B. G. Trewyn, M. P. Stellmaker, and V. S.-Y. Lin, *Angew. Chem. Int. Ed.* 44, 5038 (2005).
93. S. J. Son, J. Reichel, B. He, M. Schuchman, and S. B. Lee, *J. Am. Chem. Soc.* 127, 7316 (2005).
94. U. Schillinger, T. Brill, C. Rudolph, S. Huth, S. Gersting, F. Kroetz, J. Hirschberger, C. Bergemann, and C. Plank, *J. Magn. Magn. Mater.* 293, 501 (2005).
95. A. Ito, M. Shinkai, H. Honda, K. Yoshikawa, S. Saga, T. Wakabayashi, J. Yoshida, and T. Kobayashi, *Cancer Immunol. Immunother.* 52, 80 (2003).
96. D. K. Kim, M. S. Amin, S. Elborai, S.-H. Lee, Y. Koseoglu, M. Zahn, and M. Muhammed, *J. Appl. Phys.* 97, 10J510 (2005).
97. Y. Sun, X. Ding, Z. Zheng, X. Cheng, X. Hu, and Y. Peng, *Chem. Commun.* 2765 (2006).
98. H. A. Ferreira, F. A. Cardoso, R. Ferreira, S. Cardoso, and P. P. Freitas, *J. Appl. Phys.* 99, 08P105 (2006).
99. W. Shen, X. Liu, D. Mazumdar, and G. Xiao, *Appl. Phys. Lett.* 86, 253901 (2005).
100. P. P. Freitas, H. A. Ferreira, D. L. Graham, L. A. Clarke, M. D. Amaral, V. Martins, L. Fonseca, and J. M. S. Cabral, in "Magnetoelectronics" (M. Johnson, Ed.), New York: Academic, 2004.
101. S. I. Stoeva, F. Huo, J.-S. Lee, and C. A. Mirkin, *J. Am. Chem. Soc.* 127, 15362 (2005).
102. S. Han, T. Yu. J. Park, B. Koo, J. Joo, T. Hyeon, S. Hong, and J. Im, *J. Phys. Chem. B*, 108, 8091 (2004).
103. J. Lee, D. Lee, E. Oh, J. Kim, Y.-P. Kim, S. Jin, H.-S. Kim, Y. Hwang, J. H. Kwak, J.-G. Park, C.-H. Shin, J. Kim, and T. Hyeon, *Angew. Chem. Int. Ed.* 44, 7427 (2005).
104. A. Chachuat and B. Bonnemain, *Radiology* 35, 274 (1995).
105. R. Sheparovych, Y. Sahoo, M. Motornov, S. Wang, H. Luo, P. N. Prasad, I. Sokolov, and S. Minko, *Chem. Mater.* 18, 591 (2006).
106. F. X. Redl, K.-S. Cho, C. B. Murray, and S. O'Brien, *Nature* 423, 968 (2003).
107. T. Yang, C. Shen, Z. Li, H. Zhang, C. Xiao, S. Chen, Z. Xu, D. Shi, J. Li, and H. Gao, *J. Phys. Chem. B* 109, 23233 (2005).
108. M. Yoshitaka, N. Kazuyuki, and M. Hideki, *Small* 2, 522 (2006).
109. F. E. Osterloh, *J. Am. Chem. Soc.* 124, 6248 (2002).
110. X. Liu, L. Fu, S. Hong, V. P. Dravid, and C. A. Mirkin, *Adv. Mater.* 14, 231 (2002).
111. Q. Guo, X. Teng, S. Rahman, and H. Yang, *J. Am. Chem. Soc.* 125, 630 (2003).
112. C. Altavilla, E. Ciliberto, D. Gatteschi, and C. Sangregorio, *Adv. Mater.* 17, 1084 (2005).